1 **Exploring the ENSO Modulation of the QBO Periods with GISS E2.2 Models**

2 Tiehan Zhou[1,2], Kevin J. DallaSanta[1,3], Clara Orbe[1,3], David H. Rind[1], Jeffrey A. Jonas[1,2],

3 Larissa Nazarenko[1,2], Gavin A. Schmidt[1], Gary Russell[1]

5 [1]NASA Goddard Institute for Space Studies, New York, NY 10025, USA
6 [2]Center for Climate Systems Research, Columbia University, New York, NY 10025, USA
7 [3]Department of Applied Physics and Applied Mathematics, Columbia University, New York, NY 100-
8 25, USA

10 Correspondence to: Tiehan Zhou (tz2131@columbia.edu)

12 **Abstract.** Observational studies have shown that the El Niño–Southern Oscillation (ENSO) exerts

13 an influence on the Quasi-Biennial Oscillation (QBO). The downward propagation of the QBO tends to

14 speed up and slow down during El Niño and La Niña, respectively. Recent results from general

15 circulation models have indicated that the ENSO modulation of the QBO requires a relatively high

16 horizontal resolution, and that it does not show up in the climate models with parameterized but

17 temporally constant gravity wave sources. Here, we demonstrate that the NASA GISS E2.2 models can

18 capture the observed ENSO modulation of the QBO period with a horizontal resolution of 2° latitude by

19 2.5° longitude but with its gravity wave sources being parameterized interactively. This is because El

20 Niño events lead to more vigorous gravity wave sources generating more absolute momentum fluxes

21 over the equatorial belt, as well as less filtering of these waves into the tropical lower stratosphere

22 through a weakening of the Walker circulation. Various components of the ENSO system such as the

23 SSTs, the convective activities, and the Walker circulation are intimately involved in the generation and

24 propagation of parameterized gravity waves, through which ENSO modulates the QBO period in GISS

25 E2.2 models.

1. Introduction

The QBO dominates the interannual variability in the tropical stratosphere (Baldwin et al., 2001) while ENSO is the primary mode of interseasonal–interannual variability over the tropical Pacific Ocean (Wang et al., 2016). It is well-known that both the QBO and the ENSO have far-reaching implications for global weather and climate systems (Hamilton et al., 2015; Philander, 1990; Sarachik and Cane, 2010; Domeisen et al., 2019).

The QBO and the ENSO defy linear relationships (Angell, 1986; Xu, 1992; Hu et al., 2012) as highlighted by that fact that while the QBO and ENSO indices are negatively correlated before 1980s and positively correlated after 1980s (Garfinkel and Hartmann, 2007; Domeisen et al., 2019; Rao et al., 2020c) they are virtually uncorrelated over the longer periods from 1953 to recent times (Garfinkel and Hartmann, 2007; Geller et al., 2016b, see their Figure 5 for details). However, Maruyama and Tsuneoka (1988) spotted an intriguing connection between the anomalously short easterly phase of the QBO at 50 hPa in 1987 and the El Niño event that persisted through that year. Based on the results from a mechanistic model, Geller et. al (1997) suggested that the equatorial sea surface temperatures (SST) modulate the wave momentum fluxes into the stratosphere and thus the QBO. Remarkably, an observational study conducted by Taguchi (2010) demonstrated that the downward propagation of the QBO tends to speed up during El Niño and slow down during La Niña while the amplitude of the QBO tends to be smaller during El Niño and larger during La Niña, respectively. Using radiosonde data from 10 near-equatorial stations distributed along the Equator, Yuan et al. (2014) found that the ENSO modulation of the QBO period is more robust than that of the QBO amplitude, which is likely due to the fact that the QBO periods are characterized by a high degree of zonal uniformity whereas the QBO amplitudes exhibit the zonal asymmetries of about 10% (Hamilton et al., 2004, see their Fig. 15).

48   The QBO influences the distribution and transport of various chemical constituents (Zawodny and

49   McCormick, 1991; Trepte and Hitchman, 1992; Hasebe, 1994; Kawatani et al., 2014), the extratropical

50   circulation in the winter stratosphere (Holton and Tan, 1980; Labitzke, 1982; Rao et al., 2020a, 2020b,

51   2021), tropical moist convection (Collimore et al., 2003; Liess and Geller, 2012), the activities of tropical

52   cyclones (Gray et al., 1984; Ho et al., 2009), the ENSO (Gray et al., 1992; Huang et al., 2012; Hansen

53   et al. 2016), the Hadley circulation (Hitchman and Huesmann, 2009), the tropospheric subtropical jet

54   (Garfinkel and Hartmann, 2011a, 2011b; Kumar et al., 2022), the boreal summer monsoon (Giorgetta et

55   al., 1999; Yoden et. al 2023), and the Madden-Julian Oscillation (Yoo and Son, 2016). Thus, it is

56   imperative that weather and climate models have the capacity to simulate the ENSO modulation of the

57   QBO.

58   Various studies have investigated how the ENSO exerts its influence over the QBO in climate models.

59   Schirber (2015) conducted two sets of experiments to explore this issue using the general circulation

60   model European Centre/Hamburg 6 (ECHAM6) wherein a convection-based gravity wave (GW) scheme

61   was newly implemented. The first set of experiments was called QBOW where the initial QBO

62   configurations consisted of a westerly jet above the 10 hPa level and an easterly jet below that level.

63   Likewise, in the second set of experiments named as QBOE, the initial QBO conditions included an

64   easterly and westerly jet above and below the 10 hPa level, respectively. Schirber showed that for QBOW,

65   the ensemble mean period of the QBO from the El Niño runs is shorter than that from the La Niña runs

66   while for QBOE, the ensemble mean periods are comparable between the El Niño and the La Niña runs.

67   Schirber also noted that there is no systematic change in amplitude of the QBO jets between El Niño and

68   La Niña runs. Using version 3 of the EC-Earth Consortium's climate model with a triangular spectral

69   truncation at total wavenumber 255 (T255, horizontal resolution of ~0.54°), Christiansen et al. (2016)

70   reported that each of ten ensemble members simulated a faster QBO descent rate during El Niño than

71   during La Niña, and that their ensemble mean QBO phase speeds were comparable to those derived from

72   the reanalyses.

73   Employing two atmospheric general circulation models (AGCM) developed under the Model for

74   Interdisciplinary Research on Climate (MIROC) framework, Kawatani et al. (2019) investigated the

75   possible mechanism of the ENSO modulation of the QBO. They first compared a 100-year perpetual El

76   Niño run with a 100-year perpetual La Niña run from the MIROC-AGCM with T106 horizontal

77   resolution and 500-m vertical spacing in the stratosphere without any nonorographic GW

78   parameterizations. Then they repeated the two AMIP-style perpetual El Niño and La Niña experiments

79   but using the atmospheric part of the Model for Interdisciplinary Research on Climate, Earth System

80   Model (MIROC-ESM) with T42 horizontal resolution and 700-m vertical spacing in the stratosphere

81   where the effects of nonorographic GWs are parameterized and the GW sources are held constant in

82   time. They found that the MIROC-AGCM simulates shorter QBO periods during El Niño than during

83   La Niña because of the larger equatorial vertical wave fluxes of zonal momentum in the uppermost

84   troposphere and consequently the much larger resolved GW forcing in the stratosphere during warm

85   ENSO phase. However, they found almost no difference in the average QBO periods simulated by the

86   MIROC-ESM between El Niño and La Niña because the QBO was generated by the parameterized

87   nonorographic GW forcing in the model where the GW sources were held constant in time, thus did not

88   respond to the SST changes associated with the ENSO cycle (See their Figs. 16 and 18 for more details).

89   Using more than a dozen models from five modeling centers with their horizontal resolutions ranging

90   from T42 (~2.79°) to T1279 (~0.14°), Serva et al. (2020) found that a relatively high horizontal

91   resolution above T159 (~0.75°) was desirable to simulate the observed modulation of the QBO descent

92   rate under strong ENSO events, while the amplitude response is generally weak at any horizontal

93   resolution. They also pointed out that over-dependence on parameterizing the effects of GWs with

94 temporally invariant sources is detrimental to the realistic simulation of the coupling between the ocean

95 and the tropical stratosphere in current climate models.

96 As far as the ENSO modulation of the QBO period is concerned, both Kawatani et al. (2019) and

97 Serva et al. (2020) emphasized the importance of a relatively high horizontal resolution and the

98 inadequacy of non-interactive GW sources. However, the exploratory work of Schirber (2015) shows

99 that the ENSO modulation of the QBO period can, to some extent, be simulated in the GCM ECHAM6

100 with T63 and an associated Gaussian grid of ∼1.9° horizontal resolution because rather than being held

101 constant in time, the properties of non-interactive GW sources in the tropics are determined by the

102 simulated convection which is modulated by ENSO phases.

103 Rind et al. (1988) pioneered the use of meteorologically interactive GW sources in the Goddard

104 Institute for Space Studies (GISS) climate models. These sources included flow over topography,

105 convection, wind shear, and, in Rind et al. (2007), wind deformation. By increasing the vertical

106 resolution and revising the formulations, various versions of the GISS models subsequently simulate a

107 spontaneous QBO (Rind et al., 2014, 2020; DallaSanta et al., 2021). The GISS E2.2 models are

108 comprehensive climate models optimized for the middle atmosphere (Rind et al., 2020; Orbe et al., 2020).

109 Their outputs have been submitted to the archive of the Coupled Model Intercomparison Project Phase

110 6 (CMIP6). Bushell et al. (2020) pointed out that most of current climate models are highly dependent

111 on parameterized nonorographic GW forcing to simulate a QBO. Unsurprisingly, DallaSanta et al. (2021)

112 found that the parameterized convective GWs play a dominant role in generating the spontaneous QBO

113 in the GISS E2.2 models.

114 High-resolution AGCMs can realistically simulate atmospheric structure without resorting to

115 parameterized GWs (e.g., Watanabe et al., 2008), but the associated computational cost is too high for

116 the Earth system modeling at the present time. Thus, most climate models still require GW

117 parameterization schemes. What is more, Fig. 4(c) in Serva et al. (2020) shows that two different GW

118 parameterization schemes employed by the same T255 model make a drastic difference in the ENSO

119 modulation of the QBO period. Specifically, one scheme makes a difference of about 10 months in the

120 ensemble mean QBO period between El Niño and La Niña episodes while the other hardly makes an

121 appreciable difference. In other words, improperly parameterized GW forcing could destructively

122 interfere with the ENSO modulation of the QBO period in high-resolution climate models. Therefore, it

123 is imperative that GWs forcing be parameterized properly in climate models with a variety of horizontal

124 resolutions.

125   In this paper, we will evaluate the ENSO modulation of the QBO simulated by the GISS E2.2 models

126 against the observed and explore how the ENSO modulates the QBO period in those models. Section 2

127 describes the observations and GISS E2.2 models used in this study and outlines our methods of analyses.

128 Section 3 revisits the ENSO modulation of the QBO from the observational point of view. Section 4

129 evaluates the ENSO modulation of QBO period in the historical runs simulated by four versions of the

130 GISS E2.2 models. Section 5 explores the physical mechanisms underlying the simulated modulation.

131 Conclusions and discussion are presented in section 6.

132

133 **2. Observations, model simulations, and methods**

134 **2.1 Observations**

135   To study the observed QBO, we use the monthly mean zonal winds provided by Free University of

136 Berlin (FUB). The FUB data were produced by combining the radiosonde observations at the following

137 three equatorial stations: Canton Island near 172°W, 3°S (closed in 1967), Gan/Maledive Islands near

138 73°E, 1°S (closed in 1975), and Singapore near 104°E, 1°N (Naujokat, 1986). We use 63 years (i.e., 756

139   months) of the FUB data ranging from 1953 to 2015 at the following seven pressure levels: 70, 50, 40,

140   30, 20, 15, and 10 hPa.

141   The observed ENSO index is derived from the National Oceanic and Atmospheric Administration

142   (NOAA) Extended Reconstructed SST (ERSST) V5 datasets (Huang et al., 2017) provided by National

143   Centers for Environmental Information (NCEI). ERSST produced on a 2° × 2° grid is derived from the

144   International Comprehensive Ocean-Atmosphere Data Set (ICOADS). The latest version of ERSST,

145   version 5, uses new datasets from ICOADS Release 3.0 SST, combining information from Argo floats

146   above 5 m and Hadley Centre Ice-SST version 2 ice concentrations.

147   The monthly Outgoing Longwave Radiation (OLR) on a 2.5° × 2.5° grid from NCEI is used as a

148   proxy for tropical convection since cloud top temperatures are negatively correlated with cloud height

149   in the tropics (Salby, 2012). The ERA5 (Hersbach et al., 2020) monthly mean zonal winds were

150   employed to depict the observed Walker circulation against which we evaluate those simulated by GISS

151   E2.2 models. The employed OLR and zonal winds range from 1979 to 2015.

152   **2.2 Description of the models and simulations**

153   GISS E2.2 is a climate model specially optimized for the middle atmosphere (Rind et al., 2020; Orbe

154   et al., 2020) and its output was submitted to the Coupled Model Intercomparison Project Phase 6 (CMIP6)

155   archive. The horizontal resolution of all GISS E2.2 models is 2° (latitude) × 2.5° (longitude) for the

156   atmosphere and the model extends from the surface to 0.002 hPa (~89 km) with 102 vertical layers (for

157   more details, see Table 1 in Rind et al., 2020). Note that an adequate vertical resolution is necessary for

158   climate models to internally generate a spontaneous QBO (Scaife et al., 2000; Richter et al. 2014; Rind

159   et al, 2014, 2020; Geller et al. 2016a; Butchart et al. 2018).

160   With respect to atmospheric chemistry, the atmospheric component of the GISS E2.2 models was

161   configured in two ways for CMIP6. The first configuration is denoted as NonINTeractive (NINT) where

162 the fields of radiatively active components such as ozone and multiple aerosol species are specified from

163 previously calculated offline fields (Kelley et al. 2020; Miller et al., 2021). The second configuration

164 includes interactive gas-phase chemistry and a mass-based (One-Moment Aerosol, OMA) aerosol

165 module, where aerosols and ozone are driven by emissions and calculated prognostically (Bauer et al.,

166 2020; Nazarenko et al., 2022). The above-mentioned NINT and OMA configurations correspond to

167 physics-version=1 ("p1") and physics-version=3 ("p3"), respectively, in the CMIP6 archive.

168   The basic dynamics and tropospheric physics structure of the GISS E2.2 models were based on the

169 GISS E2.1 model (Kelley et al., 2020). One version of the cloud parameterization schemes used in E2.2,

170 termed as "standard physics" (SP), has not been fully upgraded to the state-of-the-art module customized

171 for E2.1 which has only 40 vertical layers up to 0.1 hPa (Rind et al., 2020). Accordingly, E2.2–SP has a

172 younger sibling, E2.2–AP, whose cloud parameterization schemes, termed as "Altered Physics" (AP),

173 are more aligned with those in E2.1 and whose outputs were thus favored for the submission to the

174 CMIP6 archive. "Altered Physics" in E2.2–AP brings about a somewhat different response to SST as

175 compared with the "standard physics" in E2.2–SP.

176   The QBO in the GISS models are mainly driven by GWs (DallaSanta et al., 2021). The phase

177 velocities and momentum fluxes of GW sources are coupled to convective cloud-top-pressure altitudes,

178 convective mass fluxes, background wind fields, etc. (Rind et al., 1988, 2014, 2020). Specifically

179 speaking, intrinsic phase velocities $\pm 10\ ms^{-1}$ and $\pm 20\ ms^{-1}$ of GWs generated by convection are

180 Doppler-shifted by local background winds for shallow convection and for convection penetrating above

181 the altitudes of the 400-hPa pressure level, respectively. Convective gravity wave momentum flux

182 magnitude is determined by the density and Brunt-Vaisala frequency at the top of convective region and

183 the vertically integrated mass flux over the convective region. The mass flux in the model is strongly

184 related to the depth of penetration, and thus this parameterization is somewhat similar to that of the other

185 models that use convective sources (see Eq. 7 in Rind et al., 1988 and the further discussion in Rind et

186 al., 2014).

187   Using the same GW parameterization scheme, both E2.2–SP and E2.2–AP are included in this study

188 to gain insight into the mechanisms through which ENSO modulates the QBO period despite the fact

189 that the outputs of E2.2–SP were not submitted to the CMIP6 archive.

190   We will look into two atmosphere-only (AMIP) ensemble simulations where the evolution of SST

191 and sea ice fraction (SIF) is specified and two coupled ensembles where the respective model atmosphere

192 interacts with the ocean component termed as the GISS Ocean v1 (GO1) which extends from the surface

193 to the ocean floor with 40 vertical layers and has a horizontal resolution of 1° latitude by 1.25° longitude

194 (Schmidt, et al., 2014; Kelley et al., 2020). Table 1 lists the four model configurations and their respective

195 ensemble simulations investigated in this study.

196   The first two ensembles in Table 1 were generated by AMIP–OMA–SP and AMIP–OMA–AP models

197 where the SST and SIF from the HadISST1 dataset (Rayner et al., 2003) were prescribed for the

198 simulations between 1870 and 2014 while their climatological annual cycles over the 1876–1885 period

199 were specified for the earlier simulations between 1850 and 1869. Both AMIP–OMA–SP and AMIP–

200 OMA–AP prognostically calculate the concentrations of ozone, methane, chlorofluorocarbons, aerosols,

201 etc. The main differences between AMIP–OMA–SP and AMIP–OMA–AP reside in the package of cloud

202 parameterization schemes, which leads to their different responses to SST and thus may have important

203 implications for simulating the ENSO modulation of the QBO period. We discarded the simulations

204 ranging from 1850 to 1869 in this study because they are irrelevant to the ENSO modulation of the QBO

205 in the absence of interannual variations in the prescribed SST over that period. Note that the two extended

206 historical AMIP simulations from 1870 to 2014 listed in Table 1 were not submitted to the CMIP6

207 archive. However, AMIP–OMA–AP did generate a 5-member ensemble over the 1979–2014 period that

208   was submitted to the CMIP6 archive and tagged as E2-2-G.amip.r[1-5]i1p3f1. It is worth noting that the

209   climatological characteristics over the 1979–2014 period derived from the AMIP–OMA–AP ensemble

210   listed in Table 1 are comparable to those derived from E2-2-G.amip.r[1-5]i1p3f1 albeit the climate

211   trajectories of the individual ensemble members over the 1979–2014 period are expected to differ

212   between those two ensembles starting from January 1850 and January 1979, respectively, due to the

213   chaotic nature of climate systems.

214   The other two ensembles in Table 1 were generated by the Coupled–NINT–SP and Coupled–NINT–

215   AP where the respective atmospheric components are coupled with GO1. Both the Coupled–NINT–SP

216   and Coupled–NINT–AP simulations were performed with the prescribed atmospheric composition

217   generated from the AMIP-style OMA simulations using the historical forcings over the 1850–2014

218   period. As mentioned earlier with regard to the AMIP–OMA–SP and AMIP–OMA–AP runs, the

219   difference in cloud physics between the Coupled–NINT–SP and Coupled–NINT–AP models is exploited

220   to gain a deeper insight into the mechanisms through which the ENSO modulates the QBO periods. Both

221   Coupled–NINT–SP and Coupled–NINT–AP ensemble runs started from January 1850 and ended in

222   December 2014.

223   Since there are no interannual variations in the prescribed SST over the 1850–1869 period for both

224   the AMIP–OMA–SP and AMIP–OMA–AP runs, our analyses focus on the 1870–2014 period for those

225   two ensembles. For the sake of conciseness and consistency, we also discarded the outputs from two

226   coupled runs over the 1850–1869 period. In short, we only use the data over the 1870–2014 period from

227   the ensemble simulations listed in Table 1.

228   **2.3 Methods**

229   **2.3.1 Data processing**

230   We first fill the missing FUB zonal winds at the 10 hPa level for the first 3 years by linear

231   extrapolation in log-pressure height. Then, we remove the climatological mean zonal winds from the

232   observed to obtain the monthly anomalies of zonal winds. These anomalous monthly zonal winds will

233   be used for our observational study in this paper.

234   To obtain the ENSO index from the ERSSTv5 data ranging from 1953 to 2015, we use the same

235   method to calculate the Oceanic Niño Index (ONI) as the Climate Prediction Center (CPC) of NOAA.

236   Namely, the ONI is defined as a 3-month running mean of ERSSTv5 SST anomalies in the Niño 3.4

237   region (5°S – 5°N, 120° – 170°W) based on centered 30-year base periods updated every 5 years

238   (https://origin.cpc.ncep.noaa.gov/products/analysis_monitoring/ensostuff/ONI_v5.php). This method

239   ensures a proper identification of El Niño and La Niña by taking the secular changes in SSTs into account.

240   The SST anomalies (SSTA) are defined as the deviations of the SST from its climatological annual cycle

241   over a selected base period. Specifically, the SSTA during 1951–1955 are based on the 1936–1965 base

242   period; the SSTA during 1956–1960 are based on the 1941-1970 base period; and so on. Thus, as the

243   CPC of NOAA we used the ERSSTv5 SST from January 1936 to January 2016 period to obtain the ONI

244   from January 1953 to December 2015.

245   Following the CPC of NOAA, we refer to El Niño or La Niña episodes as the periods when the ONIs

246   are greater than +0.5°C or less than –0.5°C for at least five consecutive months, respectively. Since the

247   temperature measurement is only accurate to the tenths place, all our calculated ONIs are rounded to the

248   nearest tenth. Based on the rounded ONIs, our identified El Niño and La Niña episodes are almost

249   identical to those listed at the above-mentioned website of NOAA CPC. Accordingly, we identified 21

250   El Niño and 15 La Niña events between 1953 and 2015.

251   Similarly, when we explore how GISS E2.2 models simulate the ENSO modulation of the QBO we

252   define the ONI as a 3-month running mean of prescribed SSTA from the AMIP–OMA–SP and AMIP–

253 OMA–AP runs, or simulated SSTA from the Coupled–NINT–SP and Coupled–NINT–AP runs in the

254 Niño 3.4 region (5°S– 5°N, 120°– 170°W) based on centered 30-year base periods updated every 5 years.

255 Here, the SSTA are also defined as the deviations of the SST from its climatological annual cycle over

256 a selected base period. Specifically, the SSTA during 1886–1890 are based on the 1871–1900 base

257 period; the SSTA during 1891–1895 are based on the 1876-1905 base period; the SSTA during 1991–

258 1995 are based on the 1976-2005 base period; the SSTA during 1996–2000 are based on the 1981–2010

259 base period. In addition, the SSTA during the earliest 1870–1885 and latest 2011–2014 spans are ad hoc

260 based on the 1870–1899 and 1985–2014 base periods, respectively. Thus, we used the specified or

261 simulated SSTs over the 1870–2014 period to obtain the ONI from February 1870 to November 2014.

262 For the sake of consistency, we also apply this same filtering procedure to all other fields simulated

263 by GISS E2.2 models such as OLR, zonal winds, resolved wave forcing, parameterized GW forcing,

264 absolute convective momentum flux, etc. Thus, the simulated zonal winds and other quantities were

265 subjected to a 3-month moving averaging. In addition, the secular trends of zonal winds and those other

266 quantities were also removed due to the adoption of the consecutive 5-year base periods. To further

267 simplify our analyses, all processed model outputs used in this study range from 1871 to 2013. In other

268 words, we also discarded the processed model outputs over the period between February 1870 to

269 December 1870 and that between January 2014 to November 2014.

270 Employing the above-mentioned criterion that was used to identify the observed ENSO events

271 between 1953 and 2015, we identified 34 El Niño and 30 La Niña events over the period from 1871 to

272 2013 from the specified HadISST1 dataset. We further found that the five members of the Coupled–

273 NINT–SP ensemble simulations generated 31, 31, 29, 35, and 36 El Niño events and produced 34, 34,

274 35, 37, and 35 La Niña events, respectively, over the period from 1871 to 2013. In parallel, we identified

275 37, 42, 40, 37, and 38 El Niño events and 38, 43, 37, 40, and 39 La Niña events from the SSTs simulated

276 by the five members of the Coupled–NINT–AP ensemble, respectively, over the same period.

277 **2.3.2 Statistical analysis**

278 Following Wallace et al. (1993), we decompose the zonal winds from both the observed and the

279 simulated between 10 and 70 hPa pressure levels into two leading pairs of empirical orthogonal functions

280 (EOFs) and principal components (PCs) because they typically account for more than 90% of the vertical

281 structure variance (Wallace et al., 1993; DallaSanta et al., 2021). For the sake of robustness, we excluded

282 the FUB data after 2015 because the first two EOFs explain no more than 60% of total variance during

283 the 2016 and 2019/20 QBO disruptions (Anstey et al., 2021). As a result, the QBO variability can be, to

284 a very good approximation, compactly depicted by the trajectory of $\left(PC_1(t), PC_2(t)\right)$ in a linear space

285 spanned by the first two orthonormal EOFs.

286 As in previous studies (Wallace et al., 1993; Taguchi, 2010; Christiansen et al. 2016; Serva et al.

287 2020; DallaSanta et al., 2021), the instantaneous amplitude (am) and phase (ψ) of the QBO are defined

288 as

289 $am = \sqrt{PC_1^2 + PC_2^2}$ (1)

290 $\psi = atan2(PC_2, PC_1)$ (2)

291 Differentiating (2) with respect to time yields the instantaneous phase speed of the QBO:

292 $\psi' = (PC_1 \cdot PC_2' - PC_1' \cdot PC_2)/(PC_1^2 + PC_2^2)$ (3)

293 Using Eqs. (1) – (3) and the monthly processed FUB data from 1953 to 2008, Taguchi (2010)

294 obtained 672 months of am and ψ' and partitioned each time series of $\{am\}$ and $\{\psi'\}$ into 16 categories.

295 The 16 categories correspond to the 16 combinations of four QBO phase quadrants at the 50-hPa level

296 and four seasons. Using a bootstrap (Chernick, 2007) method, Taguchi (2010) seminally illuminated the

297 annual synchronization of the QBO. Taguchi (2010) further used the bootstrap method to show that the

298 QBO signals during El Niño episodes exhibit weaker amplitude in six out of 16 categories and faster

299 phase propagation in eight out of 16 categories at a 90% or 95% confidence level (refer to Figure 6 in

300 Taguchi, 2010).

301 It is worth pointing out that while Taguchi's conclusion is physically meaningful, his statistical

302 analysis is not robust concerning the ENSO influence on the QBO. For instance, there are 18 sample

303 points in the (MAM, E) category where MAM stands for the months of boreal spring, i.e., March, April,

304 and May while E indicates the QBO winds at the 50-hPa level are easterly. As Taguchi (2010) mentioned

305 that the actual sample size should be six rather than 18 due to the data clustering. Among those 18 months

306 of data, there are six for El Niño conditions and one for La Niña condition. Also pointed out by Taguchi

307 (2010), actually sample sizes are two and one for El Niño and La Niña conditions, respectively, in the

308 (MAM, E) category. It is hard to imagine we can infer any meaningful result from one La Niña sample

309 point and two El Niño sample points out of the sample with its size being nine because Chernick (2007)

310 points out that samples of size less than 10 are usually too small to rely on sample estimates, even in

311 "nice" parametric cases, and that we should expect that such sample sizes are also too small for bootstrap

312 estimates to be of much use (see his page 174). With regard to the above-mentioned (MAM, E) category,

313 the following conclusion is evidently not robust: the QBO amplitude during El Niño episodes is weaker

314 than that during La Niña episodes at a 95% confidence level (refer to Figure 6(b) in Taguchi, 2010)

315 because one extreme La Niña and/or a couple of extreme El Niño sample points can influence the

316 outcome of the statistical test.

317 Since we have observed 21 El Niño and 15 La Niña events between 1953 and 2015, the sample sizes

318 of El Niño and La Niña appear large enough for us to conduct a classical parametric test. Namely, we

319 have two samples: one consists of 21 independent El Niño events and the other contains 15 independent

320 La Niña events. For each ENSO event, we define the amplitude [am] and phase speed [ψ'] of the QBO

321   as the monthly am in Eq. (1) and the monthly ψ' in Eq. (3) that are averaged over the number of months

322   of that event. Thus, both the El Niño sample and the La Niña sample are described by two statistics [am]

323   and [ψ'], namely the mean amplitude and mean phase speed of the QBO for an ENSO event. Note that

324   in this paper, a quantity enclosed by a pair of square brackets denotes the average value of that quantity

325   over the duration (i.e., the total number of months) of an ENSO event.

326   We employ Welch's t-test (Moser and Stevens, 1992) to infer whether there is a significant difference

327   in [am] or [ψ'] between the El Niño and La Niña population means. For the sake of conciseness, we will

328   refer to [am] and [ψ'] as A and Ψ', respectively, in this subsection and section 3. In other words, we will

329   no longer use the mnemonic notations [am] and [ψ'] in this subsection and section 3 wherein we will

330   instead employ A and Ψ', respectively, for brevity.

331   To examine whether the sample mean QBO amplitude is significantly different between El Niño and

332   La Niña, we first construct the statistic:

333    $$t = \frac{\bar{A}_1 - \bar{A}_2}{s_{\bar{A}_1 - \bar{A}_2}} \tag{4}$$

334   where $\bar{A}_1$ and $\bar{A}_2$ are the values of As that are averaged over the number of the El Niño and La Niña

335   events, respectively.

336    $$s_{\bar{A}_1 - \bar{A}_2} = \sqrt{\frac{s_{A_1}^2}{N_1} + \frac{s_{A_2}^2}{N_2}} \tag{5}$$

337   where s_{A_1} and s_{A_2} are the corrected sample standard deviation of A for El Niño and La Niña,

338   respectively while N_1 and N_2 are the sample sizes of El Niño and La Niña events. According to Moser

339   and Stevens (1992), the degrees of freedom for the t-distribution is

$$340 \quad \nu = \frac{\left(s_{A_1}^2/N_1 + s_{A_2}^2/N_2\right)^2}{\left(\frac{s_{A_1}^2}{N_1}\right)^2/(N_1-1) + \left(\frac{s_{A_2}^2}{N_2}\right)^2/(N_2-1)} \qquad (6)$$

341 **2.3.3 Analysis of the QBO forcings**

342   The QBO owes its existence to wave-mean flow interaction (Lindzen and Holton, 1968; Holton and

343 Lindzen,1972; Plumb, 1977). The evolution of zonal mean zonal winds is governed by the transformed-

344 Eulerian-mean (TEM) momentum equation formulated in pressure coordinates on a sphere (Andrews et

345 al., 1983):

$$346 \quad \frac{\partial \overline{u}}{\partial t} = \overline{G} + \frac{1}{\rho_0 a \cos\varphi} \vec{\nabla} \cdot \vec{F} - \left\{ \frac{\overline{v}^*}{a \cos\varphi} \left[\frac{\partial}{\partial\varphi}(\overline{u}\cos\varphi) - f \right] + \overline{\omega}^* \frac{\partial \overline{u}}{\partial p} \right\} + \overline{X}, \qquad (7)$$

347 where the Eliassen-Palm flux $\vec{F}$ is defined as

$$348 \quad \vec{F} = \left\{ F^{(\varphi)}, F^{(p)} \right\} = a\cos\varphi \left\{ -\overline{u'v'} + \psi\overline{u}_p, -\overline{u'\omega'} - \varepsilon[(a\cos\varphi)^{-1}(\overline{u}\cos\varphi)_\varphi - f] \right\}, \qquad (8)$$

349 and its divergence as

$$350 \quad \vec{\nabla} \cdot \vec{F} = \frac{1}{a\cos\varphi} \frac{\partial}{\partial\varphi}\left(F^{(\varphi)}\cos\varphi \right) + \frac{\partial F^{(p)}}{\partial p}. \qquad (9)$$

351 In Eq. (7), t denotes time, p pressure, φ latitude, (u, v, ω) "velocity" in (longitude, latitude, pressure)

352 coordinates, a the mean radius of Earth, ρ_0 pressure-dependent basic density, and f the Coriolis

353 parameter. In Eq. (8), ε is defined as

$$354 \quad \varepsilon = \overline{v'\theta'}/\overline{\theta}_p = -\overline{v'T'}/(\frac{\kappa\overline{T}}{p} - \frac{\partial\overline{T}}{\partial p}), \qquad (10)$$

355 where θ denotes potential temperature, T temperature, and κ the ratio of the gas constant to the specific

356 heat at constant pressure. Note that in Eqs. (7) – (10) primes denote departures from the zonal means

357 which are represented by overbars, and residual meridional and vertical velocities, i.e., $\overline{v}^*$ and $\overline{\omega}^*$, are

358 defined as $(\overline{v} - \frac{\partial\psi}{\partial p})$ and $(\overline{\omega} + \frac{1}{a\cos\varphi} \frac{\partial(\varepsilon\cos\varphi)}{\partial\varphi})$, respectively.

359   On the right hand side (RHS) of Eq. (7), the first term, $\overline{G}$, is the forcing from the GWs parameterized

360   in E2.2 models; the second term, $\frac{1}{\rho_0 a \cos \varphi} \vec{\nabla} \cdot \vec{F}$, is the forcing driven by the waves resolved by GISS

361   E2.2 models; the third term, $-\left\{ \frac{\overline{v}^*}{a \cos \varphi} \left[\frac{\partial}{\partial \varphi} (\overline{u} \cos \varphi) - f \right] + \overline{\omega}^* \frac{\partial \overline{u}}{\partial p} \right\}$, is associated with the TEM

362   advection; and last term, $\overline{X}$, is the zonal component of friction or other nonconservative mechanical

363   forcing (Andrews et al., 1987). Since $\overline{X}$ is small as far as the QBO is concerned , we will focus on

364   analyzing the first three terms of Eq. (7) and ignore the last term of that equation in this study.

365

366   **3. Revisiting the ENSO modulation of the QBO from observations**

367   In the era of big data, bootstrap methods are a powerful tool that is used to analyze uncertainties for

368   any machine learning model. However, the bootstrap methods cannot get something for nothing. It is

369   not reliable if sample size is too small. In this section, we will use the classical parametric method

370   outlined in subsection 2.3.2 to revisit the ENSO modulation of the QBO using the FUB data described

371   in subsection 2.1.

372   The solid and dashed black lines in Fig. 1 depicts the two leading EOFs derived from the monthly

373   anomalies of the FUB zonal winds between 1953 and 2015. The vertical structures of those two EOFs

374   are very similar to those depicted in Fig. 2a of Taguchi (2010) who used the FUB zonal winds from 1953

375   to 2008. Our calculated two leading EOFs account for 92.6% of the vertical structure variance (57.1%

376   by EOF1 and 35.5% by EOF2) which is slightly smaller than the value of 96.1% shown in Taguchi

377   (2010). Note that this discrepancy is not mainly due to the difference in the adopted time spans. When

378   we use the monthly anomalies of the FUB zonal winds between 1953 and 2008, the resultant two leading

379   EOFs account for 92.9% of the vertical structure variance (57.0% by EOF1 and 35.9% by EOF2). Coy

380   et al. (2020) pointed out that the descent of the QBO winds varies at intraseasonal, seasonal, and

381   interannual time scales (see their Figure 1 for more details). Thus, it is natural that two leading EOFs

382   explain more variance of the FUB zonal winds when those winds have been deseasonalized and

383   subjected to a 5-month running averaging.

384   As mentioned before, there are 21 El Niño and 15 La Niña episodes between 1953 and 2015, i.e.,

385      $N_1 = 21$ and $N_2 = 15$. Our calculations yield $\bar{A}_1 = 39.5 \, ms^{-1}$, $\bar{A}_2 = 42.4 \, ms^{-1}$, $v = 33$, and $t =$

386   -1.50. Apparently, $\bar{A}_1 < \bar{A}_2$, which suggests that the QBO amplitude is smaller during El Niño than

387   during La Niña. Performing a two-tailed test, however, we find that the QBO amplitudes during El Niño

388   episodes are not statistically different from those during La Niña episodes at the 5% significance level.

389   This is consistent with the finding of the observational study by Yuan et al. (2014), namely, the ENSO

390   modulation of the QBO amplitude is less robust than that of the QBO period. This is also consistent with

391   the findings of the modeling studies conducted by Schirber (2015) and Serva (2020).

392   Note that when we use the FUB zonal winds and the ERSSTv5 data over the 1953–2008 period as

393   Taguchi (2010), our calculations yield $N_1 = 19$, $N_2 = 13$, $\bar{A}_1 = 39.1 \, ms^{-1}$, $\bar{A}_2 = 43.1 \, ms^{-1}$, $v = 29$,

394   and $t = -1.98$. A two-tailed test shows that the difference of the QBO amplitude between El Niño and

395   La Niña is not statistically significant at the 5% significance level either.

396   Apparently, no matter whether we use the FUB data over the 1953–2008 period or over the 1953–

397   2015 period, the influence of the ENSO on the QBO amplitude is not statistically significant at the 5%

398   significance level. Thus, we will not further explore whether GISS E2.2 models can simulate the ENSO

399   modulation of the QBO amplitude in this study.

400   To examine whether the sample mean QBO phase speed is significantly different between El Niño

401   and La Niña, we similarly use Eqs. (4) – (6) except that $\bar{A}_1$ and $\bar{A}_2$ are replaced by $\overline{\Psi'_1}$ and $\overline{\Psi'_2}$,

402   respectively. Based on the data from 1953 to 2015, we obtained $N_1 = 21$ and $N_2 = 15$, $\overline{\Psi'_1} = 0.246$

403   radians/month, $\overline{\Psi'_2} = 0.183$ radians/month, $v = 28$, and $t = 2.36$. Evidently, $\overline{\Psi'_1} > \overline{\Psi'_2}$, indicating that

404 the phase speed of the QBO is greater during El Niño than during La Niña. Performing a two-tailed test,

405 we ascertain that the phase speed of QBO during El Niño episodes are statistically different from those

406 during La Niña episodes at the 5% significance level. Put in another way, the mean QBO period of 25.6

407 months (i.e., $2\pi/0.246$) during El Niño is statistically shorter than that of 34.3 months (i.e., $2\pi/0.183$)

408 during La Niña over the 1953–2015 period. Furthermore, when we use the FUB zonal winds and the

409 ERSSTv5 data over the 1953–2008 period as Taguchi (2010), our calculations yield $N_1 = 19$ and $N_2 = $

410 13, $\overline{\Psi_1'} = 0.253$ radians/month, $\overline{\Psi_2'} = 0.180$ radians/month, $\nu = 25$, and $t = 2.87$. Apparently, we

411 reach a similar conclusion that the mean QBO period of 24.8 months (i.e., $2\pi/0.253$) during El Niño is

412 statistically shorter than that of 34.9 months (i.e., $2\pi/0.180$) during La Niña at the 5% significance level.

413   Thus, no matter whether we use the FUB data over the 1953–2008 period or over the 1953–2015

414 period, the influence of the ENSO on the QBO phase speed is statistically significant at the 5%

415 significance level. In other words, our observational study robustly buttresses the following conclusion

416 of Taguchi (2010): the QBO descent is faster during El Niño than during La Niña. Henceforth, we will

417 focus only on the ENSO modulation of the QBO period in this study.

418   To facilitate comparison with other studies (e.g., Taguchi, 2010; Christiansen et al., 2016; Serva et

419 al. 2020), we also calculate the mean phase speed of the QBO by averaging monthly ψ' in Eq. (3) over

420 all the 210 months of the El Niño episodes and over all the 201 months of the La Niña episodes between

421 1953 and 2015. Subsequently, we obtain the mean QBO period of 25.6 months during El Niño and of

422 32.2 months during La Niña for the 1953–2015 period. Similarly, we obtain the mean phase speed of the

423 QBO by averaging monthly ψ' in Eq. (3) over all the 186 months of the El Niño episodes and over all

424 the 174 months of the La Niña episodes for the 1953–2008 period. The resultant values are 24.9 and 32.2

425 months, respectively, which are very close to 25 and 32 months inferred by Taguchi (2010). No matter

426   whether the selected FUB data span from 1953 to 2008 or range from 1953 to 2015, we robustly conclude

427   that the QBO descent rate is faster during El Niño than during La Niña.

428   Note that it is difficult to rigorously determine the degrees of freedom for a t-test when we choose the

429   monthly data as sample points which share some common characteristics, i.e., are not independent of

430   each other during an ENSO event (for more details, refer to Taguchi, 2010). In the remainder of this

431   paper, when we need to conduct a Welch's t-test we choose the QBO period averaged over each ENSO

432   episode as a sample point. Otherwise, the mean values during El Niño or La Niña are referred to the

433   quantities averaged over all the months of El Niño or La Niña category in alignment with previous works

434   conducted by Taguchi (2010), Christiansen et al. (2016), and Serva et al. (2020).

435   The QBO is mainly driven by tropical waves (Lindzen and Holton, 1968; Holton and Lindzen, 1972;

436   Plumb 1977) of which tropical convection is an important source (Holton, 1972; Salby and Garcia, 1987;

437   Bergman and Salby, 1994; Tsuda et al., 2009; Alexander et al., 2017). To investigate how tropical

438   convection is influenced by the ENSO, we first produce the monthly anomalies of OLR from NOAA

439   NCEI over the 1979–2015 period. Then we obtain the mean OLR anomalies (OLRA) for La Niña and

440   El Niño conditions by averaging the monthly OLRA over all the months that fall into La Niña and El

441   Niño categories, respectively. Fig. 2a show that mean OLRA exhibit a broad and positive pattern that

442   spans the central and eastern equatorial Pacific and a negative pattern in the maritime continent for the

443   La Niña conditions. In contrast, Fig. 2b show that they exhibit a broad and negative pattern that spans

444   the central and eastern equatorial Pacific and a positive pattern in the maritime continent for the El Niño

445   conditions. The large differences in the mean OLRA in Fig. 2c between El Niño and La Niña conditions

446   are closely related with the contrast in the SSTA patterns shown in Fig. 3. Namely, the distinctive

447   patterns of positive and negative SSTA extend over the central and eastern Pacific during the El Niño

448   and La Niña episodes, respectively, which not only gives rise to the corresponding positive and negative

449   rainfall anomalies (Philander, 1990) and the concomitant OLRA shown in Fig. 2, but also leads to

450   various teleconnections outside the tropics (Domeisen et al., 2019).

451   In order to test whether the difference patterns of OLRA and SSTA shown in Figs. 2c and 3c are

452   statistically robust we use [OLRA] and [SSTA] as our sample points to perform two-tailed tests. Figs.

453   S1 and S2 shown in the supplement demonstrate that the difference patterns are statistically significant

454   at the 5% significance level.

455   In the next section, we will evaluate how the ENSO modulates the QBO periods in the E2.2 models

456   and whether those models can realistically capture the contrast in the OLR (and convection) patterns that

457   generally underlies the difference in wave driving of the QBO between warm and cold ENSO conditions.

458

459   **4. ENSO modulation of the QBO period in GISS E2.2 models**

460   Now we investigate the ENSO modulation of the QBO period in the ensemble simulations listed in

461   Table 1.

462   We first calculate the monthly mean anomalies of zonal winds using the method outlined in

463   subsection 2.3.1. Then we average those monthly mean anomalous zonal winds over the latitudinal belt

464   from 5° S to 5° N to obtain the monthly QBO winds over the 1871 to 2013 period at the following seven

465   pressure levels: 70, 50, 40, 30, 20, 15, and 10 hPa.

466   As in section 3, we decompose the QBO winds from 10 to 70 hPa over the 1871–2013 period into

467   two leading pairs of empirical orthogonal functions (EOFs) and principal components (PCs). For each

468   of the 19 ensemble simulations listed in Table 1, the first two leading EOFs account for at least 92.9%

469   of the vertical structure variance which is comparable to the value derived from the observations

470   discussed in section 3. Since coupled models encounter more difficulties in simulating the ENSO

471   modulations of the QBO (Serva et al. 2020, see their Fig.4 for more details), we first look into the

472   ensemble simulations from the Coupled–NINT–AP model, which incorporates the most up-to-date cloud

473   parameterization schemes. The red and blue lines in Fig. 1 depicts the first two leading EOFs from each

474   of all five Coupled–NINT–AP runs. For each of those five runs, the first two leading EOFs account for

475   at least 93.8% of the vertical structure variance. The vertical structures of those two EOFs from each

476   Coupled–NINT–AP run are broadly similar to the solid and dashed black lines derived from observations

477   in Fig. 1. The respective vertical structures of the first two leading EOFs are almost identical among all

478   five Coupled–NINT–AP ensemble runs, which is expected because all runs share the same model and

479   differ from each other only in their initial conditions. It is worth noting that the vertical structures of the

480   first two leading EOFs simulated by Coupled–NINT–AP are somewhat different from those observed

481   below the 20 hPa level because none of CMIP models could simulate a QBO in the lower stratosphere

482   that is as strong as the observed (Richter et al., 2020). In addition, we find that the vertical structures of

483   the first two leading EOFs from other three ensemble simulations listed in Table 1 (figures not shown)

484   are comparable to those from the Coupled–NINT–AP runs.

485   For the ensemble simulations listed in Table 1, we define an El Niño or La Niña event according to

486   the criterion described in subsection 2.3.1. Similarly, Eq. (3) is used to calculate the instantaneous (i.e.,

487   monthly) phase speed of the simulated QBO. For each El Niño or La Niña event, the mean phase speed

488   of the simulated QBO from any individual run listed in Table 1 is obtained by averaging the

489   instantaneous phase speeds of the simulated QBO over the number of months of that event. Accordingly,

490   we have one sample consisting of independent El Niño events and the other consisting of independent

491   La Niña events. In addition, we employ a two-tailed Welch's t-test outlined in subsection 2.3.2 to

492   examine whether there is a significant difference in the phase speed of the simulated QBO between the

493   El Niño and La Niña population means.

494   Table 2 describes how the ENSO influence the QBO period in each member of all ensembles, where

495   E[1-4] represent AMIP–OMA–SP, AMIP–OMA–AP, Coupled–NINT–SP, and Coupled–NINT–AP

496   ensembles, respectively while r1, r2,… indicate its respective member of each ensemble. As we

497   mentioned in subsection 2.3.1, for the member r1 of E1, i.e., the first run of the AMIP–OMA–SP

498   ensemble, there are 34 El Niño and 30 La Niña events between 1871 and 2013, i.e., $N_1 = 34$ and $N_2 =$

499   30 in Eqs. (5) and (6). Then we obtained the phase speed of the QBO for each episode of those 34 El

500   Niño and 30 La Niña events, from which we derived the mean phase speed of the QBO averaged over

501   the 34 El Niño and 30 La Niña events, respectively. Accordingly, our mean phase speeds of the QBO

502   simulated by r1 of E1 averaged over the El Niño and La Niña events are obtained as 0.202 radians/month

503   and 0.185 radians/month, respectively, and the standard deviations about those mean phase speeds as

504   0.0345 radians/month and 0.0275 radians/month, respectively. Substituting those numbers into

505   Eqs. $(4) - (6)$ yields $\nu = 61$, and $t = 2.25$. Therefore, the phase speed of the QBO simulated by r1 of

506   E1 is statistically significantly greater during El Niño than during La Niña at the 5% significance level.

507   Accordingly, we register the mean QBO period of 31.1 months (i.e., $2\pi/0.202$) during the El Niño

508   episodes and 34.0 months (i.e., $2\pi/0.185$) during the La Niña episodes as the entries for r1 of E1 in

509   Table 2. Since the phase speeds of the QBO simulated by r1 of E1 are statistically significantly different

510   between the El Niño and La Niña categories at the 5% significance level, we can regard the QBO periods

511   as being statistically significantly different between El Niño and La Niña episodes and register their

512   difference, -2.9 months, in Table 2 with a pair of parentheses indicating this significance. Similarly, we

513   calculated the QBO periods during ENSO extremes and their difference simulated by every member of

514   all ensembles and registered them in Table 2 where the numbers in the parentheses indicate that the

515   phase speed of the simulated QBO is statistically significantly greater during El Niño than during La

516   Niña at the 5% significance level.

517   Table 2 shows that 18 of 19 runs from the four GISS E2.2 models listed in Table 1 can simulate the

518   ENSO modulation of the QBO period discussed in section 3. For each Coupled–NINT–AP ensemble

519   run, the phase speed of the simulated QBO is statistically significantly greater during El Niño than during

520   La Niña at the 5% significance level. For the AMIP–OMA–SP and AMIP–OMA–AP ensembles, most

521   members also generate a spontaneous QBO whose phase speed is statistically significantly greater during

522   El Niño than during La Niña at the 5% significance level. Intriguingly, in none of the Coupled–NINT–

523   SP ensemble runs is the phase speed of the simulated QBO statistically significantly different between

524   El Niño and La Niña episodes at the 5% significance level albeit the contrast in the QBO periods between

525   the two categories simulated by r1 of E3 (i.e., Coupled–NINT–SP) is equal to -6.2 months and greater

526   than that simulated by most members of Coupled–NINT–AP. We will look further into this issue in

527   section 6.

528   **5. Mechanisms of the ENSO modulation of the QBO period in GISS E2.2 models**

529   **5.1 ENSO modulation of the QBO forcings**

530   Section 4 shows that the ENSO modulation of the QBO period can be simulated by each of the AMIP–

531   OMA–SP, AMIP–OMA–AP, and Coupled–NINT–AP models. The difference in the phase speed of the

532   simulated QBO between ENSO extremes is statistically significant at the 5% significance level for most

533   of those model runs. For Coupled–NINT–SP, one of its historical runs exhibits an opposite response,

534   namely, the simulated QBO propagates downward slower during El Niño than during La Niña while

535   other four runs from the identical model configuration do bring about a faster phase speed of the QBO

536   during warm ENSO events. However, no matter whether the difference in the QBO period simulated by

537   Coupled–NINT–SP is positive or negative between ENSO extremes, it is not statistically significant at

538   the 5% significance level. In this section, we start with investigating how the first three terms in Eq. (7),

539   i.e., the parameterized GW forcing, the resolved wave forcing, and the TEM advection, respond to ENSO

540   extremes and how their evolutions are related with those of the simulated QBO winds.

541   As shown in sections 3 and 4, both the observed and simulated QBO can be very well represented by

542   the trajectory of $\left(PC_1(t), PC_2(t)\right)$ in a linear space spanned by the first two orthonormal EOFs. In other

543   words, at any time t, the QBO wind profile, $U'_{profile}$ is very close to the following linear combination:

544    $PC_1(t) \cdot EOF_1 + PC_2(t) \cdot EOF_2$. Here, the QBO wind, U', refers to the deseasonalized and smoothed

545   monthly mean zonal winds averaged over the zonal belt from 5° S to 5° N. We construct the composite

546   fields of the QBO winds, the GW forcing, the resolved wave forcing, and the TEM advection according

547   to the phase angle of the QBO wind profiles. For each month that falls into the El Niño or La Niña

548   category, we use Eq. (2) to calculate the phase angle of the QBO wind profile, each cycle of which over

549   the 1871–2013 period is divided into 24 bins with the bin size of 15°. Note that if two QBO wind profiles

550   belong in the same bin, they look similar because any one of them can be approximated by the other

551   multiplied by a scalar factor. Therefore, for each of the El Niño and La Niña categories, it is very natural

552   for us to generate the composite QBO winds for that category by averaging all wind profiles in each bin

553   and produce the concomitant composite fields of the GW forcing, the resolved wave forcing, and the

554   TEM advection in the corresponding bin.

555   Fig. 4 depicts the composite fields of the QBO winds (black contours) and parameterized (left panels)

556   and resolved (right panels) wave forcing averaged over all realizations of the Coupled–NINT–AP

557   ensemble. All composite fields in this section have been subjected to the averaging over the latitudinal

558   belt from 5°S to 5°N. The ensemble average is achieved on the basis that the respective vertical

559   structures of the first two leading EOFs are almost identical among all five Coupled–NINT–AP ensemble

560   runs as demonstrated in Fig. 1. Both Figs. 4a and 4b show a characteristic feature of the QBO. Namely,

561   the maximum eastward and westward wave forcing from parameterized GWs are located below and

562   propagate downward with the westerly and easterly QBO jets. Fig. 4c reveals the stronger parameterized

563   GW forcing in both eastward and westward shear zones of the QBO winds during El Niño than during

564   La Niña, which gives rise to the faster phase speed of the QBO during warm ENSO episodes than during

565   its cold counterparts. Figs. 4d and 4e show that the relationship between resolved wave forcing and the

566   QBO winds are somewhat more complex. When zonal wind anomalies are close to zero, the coherent

567   and modest resolved westward wave forcing helps the easterly shear zone of the QBO winds to propagate

568   downwards from the 10 hPa level to the 70 hPa level during both the cold and warm ENSO episodes

569   while the coherent and modest resolved eastward wave forcing helps the westerly shear zone of the QBO

570   winds to propagate downwards only from the 20 hPa level to the 70 hPa level during both the cold and

571   warm ENSO episodes. At altitudes above the 20 hPa level, easterly jet cores are modestly weakened by

572   the resolved eastward wave forcing during the two extreme ENSO phases. In particular, Fig. 4f indicates

573   that at altitudes above the 30 hPa level the response of the resolved wave forcing to the ENSO acts to

574   slow down the downward propagation of the QBO during El Niño than during La Niña. However, the

575   parameterized GW forcing shown in Fig. 4 clearly dominates over the resolved wave forcing, which is

576   consistent with the finding of DallaSanta et al. (2021) that the parameterized convective GWs play a

577   dominant role in generating the spontaneous QBO in the GISS E2.2 models.

578   Figs. 5a–5c depict the composite fields of the QBO winds (black contours) and TEM advection

579   averaged over all realizations of the Coupled–NINT–AP ensemble. Comparing Figs. 5a–5c with Fig. 4

580   reveals that the TEM advection composite is also larger than composite resolved wave forcing in the

581   Coupled–NINT–AP model. Thus, the QBO simulated by this model is intimately related to the

582   parameterized GW forcing and the TEM advection. It is well-known that while wave forcing is largely

583   balanced out by the TEM advection in the extratropical stratosphere (Haynes, et al., 1991) tropical wave

584   forcing not only drives internal variabilities of zonal winds but also cancel out the TEM advection in the

585 stratosphere (Scott and Haynes, 1998). Figs. 5a–5b also show that the maximum positive and negative

586 advective tendencies are located above rather than below and propagate downward with the westerly and

587 easterly QBO jets, thus acting to slow down the downward propagation of the QBO, which is mainly

588 caused by the persistent tropical upwelling and a general feature of the QBO (Giorgetta et al. 2006; Rind

589 et al., 2014). Fig. 5c indicates that there exist stronger positive and negative advective tendencies above

590 the westerly and easterly QBO jets during El Niño than during La Niña. In other words, the TEM

591 advection alone leads to a slower phase speed of the QBO during El Niño than during La Niña. This is

592 not surprising because El Niño gives rise to a stronger tropical upwelling in the lower stratosphere (Calvo

593 et al., 2010; Simpson et al., 2011; Domeisen et al., 2019).

594 Figs. 5d–5f show the composite QBO winds (black contours) and the composite sum of parameterized

595 GW forcing, resolved wave forcing, and TEM advection averaged over all realizations of the Coupled–

596 NINT–AP ensemble. In other words, the upper, middle, and lower panels depict the sum of the fields

597 shown in all the corresponding panels of Fig. 4 and Figs. 5a–5c. The pattern of the composite sum is

598 generally determined by the pattern of parameterized GW forcing even though the latter is more coherent

599 than the former. Thus, we conclude that the shorter QBO period during El Niño simulated by Coupled–

600 NINT–AP is mainly caused by stronger parameterized GW forcing during warm ENSO episodes. We

601 also find that stronger parameterized GW forcing during warm ENSO events are simulated by AMIP–

602 OMA–SP and AMIP–OMA–AP models (figures not shown), which helps us understand why most

603 members from each of those three ensembles generate a spontaneous QBO whose phase speed is

604 statistically significantly greater during El Niño than during La Niña at the 5% significance level.

605 Now we explore how ENSO influences parameterized GW forcing, resolved wave forcing, and TEM

606 advection simulated by the Coupled–NINT–SP model, i.e., the remaining model listed in Tables 1 and

607 2. Contrasting between Fig. 6a and Fig. 4c reveals that the ensemble mean composite response to the

608 ENSO of parameterized GW forcing simulated by Coupled–NINT–SP is substantially weaker than that

609 simulated by Coupled–NINT–AP. Although the Coupled–NINT–SP simulations still bring about

610 enhanced westward parameterized GW forcing in the easterly shear zones of the simulated QBO winds

611 during El Niño in contrast to La Niña, the magnitude of the reinforcement is only about two thirds of

612 that simulated by Coupled–NINT–AP. In particular, in Fig. 6a there is no coherent pattern of enhanced

613 eastward parameterized GW forcing in the westerly shear zones of the QBO winds simulated by

614 Coupled–NINT–SP, which is in glaring contrast to the coherent pattern of positive enhancement shown

615 in Fig. 4c generated from the Coupled–NINT–AP ensemble. Figs. 6b and 6c show that both resolved

616 wave forcing and TEM advection respond to the ENSO weakly and uniformly in the Coupled–NINT–

617 SP ensemble simulations. Combining all three composite fields together, Fig. 6d demonstrates that the

618 ensemble mean of the Coupled–NINT–SP simulations still simulates a coherent but much weaker

619 response to the ENSO of resultant forcing at altitudes above the 40 hPa level, which helps us to explain

620 why only some of the Coupled–NINT–SP ensemble runs can simulate a faster QBO descent rate during

621 El Niño than during La Niña and the ENSO does not make a difference in the phase speed of the QBO

622 that is statistically significant at the 5% significance level in any of those Coupled–NINT–SP runs.

623 **5.2 ENSO modulation of the generation and propagation of parameterized gravity waves**

624 A natural question that arises is how the parameterized GW forcing relates to the SSTA of ENSO

625 extremes specified in or simulated by the GISS E2.2 models listed in Table 1. Figs. 7a and 7b show the

626 ensemble averages of the composite SSTA averaged over all La Niña and El Niño months respectively

627 over the 1871–2013 period simulated by Coupled–NINT–AP. Comparing Figs. 7a and 7b with Figs. 3a

628 and 3b reveals that the amplitude of the ENSO simulated by Coupled–NINT–AP is larger than the

629 observed. Figs. 7c and 7d show the differences between the simulated SSTA arising from the ENSO

630 events shown in Figs. 7a and 7b and the observed SSTA shown in Figs. 3a and 3b, indicating that the

largest discrepancies occur over the western and eastern equatorial Pacific. Figs. 7a and 7b also demonstrate that the model has a capability to simulate the ENSO amplitude asymmetry (Cane and Zebiak, 1987; Yu and Mechoso, 2001), namely, the amplitudes of the ENSO are relatively larger during warm episodes than during cold episodes. As in Fig. 3 of Zhao and Sun (2022), Fig. 7e depicts the sum of the composite SSTA shown in Figs. 7a and 7b that they used to characterize the ENSO amplitude asymmetry while Fig. 7f shows their difference. Their Fig. 3 reveals that most CMIP6 models cannot simulate the pattern of a positive residual in the sum of the composites of ENSO extremes in the tropical eastern Pacific. Further comparison between Fig. 3 in Zhao and Sun (2022) and Fig. 7e indicates that the ENSO amplitude asymmetry simulated by Coupled–NINT–AP is only about 50% of that simulated by the GISS-E2-1-H model discussed in their study whose ENSO amplitude asymmetry is comparable to the observed.

Since this study is chiefly concerned with the ENSO modulation of the QBO period, we focus on the ensemble mean difference between the composite SSTA of ENSO extremes, which can be interpreted as the trough-to-crest amplitude of the ENSO cycle. Comparing Fig. 8a with Fig. 3c indicates that the trough-to-crest ENSO amplitude derived from the HadISST1 dataset over the 1871–2013 period is somewhat smaller than that derived from the ERSSTv5 dataset over the 1953–2015 period, which is consistent with the finding by Grothe et al. (2019) that the increase in the ENSO variability is statistically significant (>95% confidence) from the preindustrial to recent era, no matter whether the latter is defined by the previous 30, 50, 75, or 100 years before 2016. Fig. 7f and Fig. 8 also reveal that the ENSO amplitude simulated by Coupled–NINT–AP is substantially greater than that simulated by Coupled–NINT–SP, which was previously revealed in Rind et al. (2020). The tendency to generate stronger ENSO oscillations means that the Coupled-NINT-AP runs will also more readily exceed the $\pm0.5°C$ criteria for El Niño and La Niña events, and the Coupled–NINT–AP runs do simulate more ENSO events over

654 the 1871–2013 period than the Coupled–NINT–SP runs as indicated in subsection 2.3.1. Fig. 8 further

655 shows that the ENSO amplitude simulated by Coupled–NINT–SP is noticeably greater than those

656 specified in the AMIP–OMA–SP and AMIP–OMA–AP models (which, being derived from observations,

657 are identical) even though it is substantially weaker than that simulated by Coupled–NINT–AP.

658   We also ascertain that the Hadley circulation simulated by each of the four models listed in Table 1

659 strengthens and weakens during warm and cold ENSO episodes respectively (figure not shown), which

660 is consistent with the finding by Oort and Yienger (1996).

661   Schirber (2015) discovered that the parameterized GW mean momentum source is about 15% larger

662 in the El Niño ensemble than in the La Niña ensemble because the El Niño leads to enhanced

663 precipitation and convective heating. Similarly, we calculate the absolute value of convective

664 momentum fluxes (ACMF) at the source altitude and composite the ACMF anomalies averaged over the

665 latitudinal belt between 5°S and 5°N from El Niño and La Niña categories respectively over the 1871–

666 2013 period. Fig. 9 shows the composite difference in the equatorial mean ACMF anomalies between El

667 Niño and La Niña over the 1871–2013 period, indicating that the absolute momentum fluxes at the source

668 levels over the equatorial belt is larger during El Niño episodes than during La Niña episodes for each

669 of 19 runs listed in Table 1. This finding is consistent with that of Geller et al. (2016b), Alexander et al.

670 (2017), and Kang et al. (2018), namely, both convective GW momentum fluxes and convective GW

671 wave forcing are generally stronger during El Niño than during La Niña in the equatorial region. The

672 ensemble mean difference in the absolute momentum fluxes at the source levels averaged over that

673 equatorial belt between El Niño and La Niña is obtained as 0.07, 0.15, 0.10, and 0.12 mPa for AMIP–

674 OMA–SP, AMIP–OMA–AP, Coupled–NINT–SP, and Coupled–NINT–AP, respectively. Note that

675 these composite differences in ACMF between El Nino and La Nina translate into ACMF being about

676 10-20% larger in the El Niño ensembles than in the La Niña ensembles, thus agree with the Schirber

677 (2015). Since the QBO period is inversely dependent upon the momentum flux (Plumb, 1977), the

678 differences in equatorial absolute momentum fluxes at the source altitude contribute to shortening and

679 lengthening of the simulated QBO period during warm and cold ENSO phases, respectively.

680   Fig. 3 shows that the locations of warmest SSTs shift from the maritime continent during La Niña

681 episodes to the central and eastern equatorial Pacific during El Niño episodes. Since strong convective

682 activities over tropical oceans are generally located above the regions where the SSTs exceed 26°– 28° C

683 (Graham and Barnett, 1987; Zhang, 1993), strong convective activities also shift eastward from cold to

684 warm ENSO phases, as illustrated in Fig. 2. Using satellite data, the climatological study by Sullivan et

685 al. (2019) demonstrated that the occurrence of organized deep convection during El Niño events

686 increases threefold in the central and eastern Pacific and decreases twofold outside of these regions in

687 contrast to that during La Niña events. It is well-established that the Walker circulation strengthens

688 during La Niña and weakens during El Niño (Bjerknes, 1969).

689   Next, we construct the equatorial zonal winds as the zonal winds averaged from 5°S to 5°N. Then we

690 define the equatorial winds during La Niña and El Niño as the equatorial winds averaged over all months

691 that fall into the La Niña and El Niño categories, respectively. Fig. 10 illuminates that the Walker

692 circulation derived from ERA5 reanalysis during El Niño is substantially weaker than its counterpart

693 during La Niña over the equatorial Pacific and the eastern equatorial Indian ocean. Particularly in the

694 upper equatorial troposphere, the westerlies above the central and eastern Pacific during El Niño

695 episodes are decreased by more than 50% as compared with those during La Niña ones while the

696 easterlies above the equatorial Indian ocean and the maritime continent during El Niño conditions are

697 weakened by more than 30% as compared with those during La Niña ones. Kawatani et al. (2019) argue

698 that the weaker upper tropospheric winds during El Niño episodes enable a greater amount of GW

699 momentum fluxes to be transferred from the troposphere into stratosphere because less GWs are filtered

out. This argument assumes critical-level absorption of otherwise weakly damped, vertically propagating GWs, which was adopted by Lindzen and Holton (1968). The weaker Walker circulation leads to a shorter QBO period during El Niño while the stronger Walker circulation results in a longer QBO period during La Niña.

Fig. 11 depicts the ensemble mean composite difference in the equatorial zonal wind anomalies between warm and cold ENSO extremes simulated by the E2.2 models listed in Table 1. The patterns of the simulated wind anomalies shown in Fig. 11 are very similar to that derived from the ERA5 reanalysis shown in Fig. 10c. Namely, the weakened Walker circulation simulated by the E2.2 models during El Niño episodes results in weaker upper tropospheric westerlies over the central and eastern equatorial Pacific and weaker upper tropospheric easterlies over the maritime continent and equatorial Indian ocean while the intensified Walker circulation simulated by the E2.2 models during La Niña episodes leads to stronger upper tropospheric westerlies over the central and eastern equatorial Pacific and stronger upper tropospheric easterlies over the maritime continent and equatorial Indian ocean. The difference in the wind filtering of upward propagating GWs causes a greater transfer of GW momentum fluxes into the tropical stratosphere during El Niño episodes than during La Niña episodes, leading to a shorter QBO period during El Niño events than during La Niña events. Fig. 11 reveals that the maximum contrast in the upper tropospheric zonal winds between warm and cold ENSO extremes simulated by two AMIP models, i.e., AMIP–OMA–SP and AMIP–OMA–AP, reaches -13.1 ms^{-1} and -12.1 ms^{-1}, respectively, over the central and eastern equatorial Pacific, and attains 6.6 ms^{-1} and 6.4 ms^{-1}, respectively, over the maritime continent and equatorial Indian ocean. Those maximum contrasts are somewhat smaller than what is derived from the ERA5 reanalysis shown in Fig. 10, namely -15.0 ms^{-1} over the central and eastern equatorial Pacific and 7.8 ms^{-1} over the maritime continent and equatorial Indian ocean. However, the maximum contrast in the upper-tropospheric zonal winds over the central and eastern

equatorial Pacific between warm and cold ENSO extremes simulated by two coupled ocean-atmosphere models, i.e., Coupled–NINT–SP and Coupled–NINT–AP, only reaches -7.5 ms^{-1} and -8.2 ms^{-1}, respectively, thus is substantially smaller than that derived from the ERA5 reanalysis. Meanwhile, the maximum contrast in the upper-tropospheric zonal winds over the maritime continent and equatorial Indian ocean between warm and cold ENSO extremes simulated by those two coupled models, reaches 7.0 ms^{-1} and 10.3 ms^{-1}, respectively, which is slightly smaller than and somewhat larger than the observed values, respectively.

The comparison of the observed and simulated changes in the Walker circulation between warm and cold ENSO extremes shown in Figs. 10 and 11 can both account for a shorter QBO period simulated by all GISS E2.2 models and explain why the two AMIP models can better capture the ENSO modulation of the QBO period than the Coupled–NINT–SP model as indicated in Table 2. However, it can neither explain why the Coupled–NINT–AP model can capture the ENSO modulation of the QBO period as two AMIP models nor illuminate why the coupled model with the altered physics (i.e., Coupled–NINT–AP) performs better than the coupled model with the standard physics (i.e., Coupled–NINT–SP). Further comparing the simulated SST changes between warm and cold ENSO extremes shown in Figs. 7 and 8 hints that the unduly amplified ENSO in the coupled AP runs holds the key to those unsettled issues that is detailed as follows.

Using a large ensemble of multiple climate models, Serva et al. (2020) discovered that the AMIP historical runs generally better capture the ENSO modulation of the QBO period than the coupled ocean-atmosphere historical simulations. In particular, among a few coupled ocean-atmosphere models that do, to various extents, capture the ENSO modulation of the QBO period, the common feature is that each of them can largely simulate the observed OLR anomaly pattern shown in Fig. 2c albeit the magnitudes of those simulated OLRA from their historical runs are roughly 50% stronger than the observed (for more

746   details, refer to their Fig. 8 in Serva et al., 2020). For the sake of comparison, we construct the ensemble

747   mean composite difference in the OLRA between warm and cold ENSO extremes in the same way we

748   constructed the ensemble mean composite difference in the zonal wind anomalies depicted in Fig. 11.

749   Figs. 12a and 12b show that the patterns of the OLRA simulated by AMIP–OMA–SP and AMIP–

750   OMA–AP largely resemble the observed one shown in Fig. 2c. Although the pattern simulated by

751   AMIP–OMA–AP matches better with the observed, the convective activities during El Niño episodes

752   simulated by AMIP–OMA–SP and AMIP–OMA–AP are apparently inadequate over the region where

753   the upper tropospheric westerlies weaken most conspicuously during warm ENSO extremes shown in

754   Figs. 11a and 11b, respectively. Thus, although the contrast in the wind filtering of GWs between El

755   Niño and La Niña episodes simulated by the two AMIP E2.2 models are comparable to the observed,

756   the difference in the GW momentum flux transferred into the equatorial stratosphere between warm and

757   cold ENSO extremes may well be smaller than the observed with the correct SSTs. This partly explains

758   why the contrast between the observed mean QBO period during El Niño episodes (i.e., 25.6 months)

759   and the observed mean QBO period during La Niña episodes (i.e., 34.3 months) is higher than that

760   simulated by the two AMIP models shown in Table 2 (i.e., E1 and E2 in Table 2). As exhibited by the

761   coupled model capable of simulating the ENSO modulation of the QBO period, Fig. 12d shows that the

762   contrast in the OLRA between warm and cold ENSO extremes simulated by Coupled–NINT–AP is

763   apparently sharper than the observed one shown in Fig. 2c. In particular, the tropical convection in the

764   central and eastern Pacific during El Niño episodes simulated by Coupled–NINT–AP is both more

765   extensive and more intensive than that simulated by the two AMIP models shown in Figs. 12a and 12b,

766   which is consistent with the fact that the composite contrast in the SSTA simulated by Coupled–NINT–

767   AP shown in Fig. 7d is substantially sharper than that prescribed in the two AMIP models shown in Fig.

768   8a. Thus, even though the wind filtering of GWs during El Niño episodes simulated by Coupled–NINT–

AP shown in Figs 12d is significantly smaller than that simulated by AMIP–OMA–SP and AMIP–OMA–AP shown in Figs 12a and 12b, respectively, the combined effect of the lower contrast in the wind filtering and the higher contrast in the amount of GW momentum fluxes generated by convective activities between warm and cold ENSO extremes over the central and eastern tropical Pacific results in a comparable ENSO modulation of the QBO period simulated by Coupled–NINT–AP to that simulated by the two AMIP models as illustrated in Table 2.

Finally, comparing Fig. 12c with Fig. 2c and other three panels in Fig. 12 reveals that convective activities during the warm ENSO phase simulated by the Coupled–NINT–SP model are substantially weaker than both the observed and those simulated by other three models list in Table 1. Combining the small composite OLR difference shown in Fig. 12c and the small difference in the wind filtering shown in Fig. 8c between warm and cold ENSO extremes over the central and eastern equatorial Pacific results in a low contrast in GW forcing between warm and cold ENSO phases shown in Fig. 6a, which, short of the compensating effect of the excessively amplified ENSO in Coupled–NINT–AP ensemble runs, should lead to a relatively weaker ENSO modulation of the QBO period simulated by the Coupled–NINT–SP model as illustrated in Table 2. However, this is not the whole story; and we will return to this subject in the discussion section[1].

6. Discussion and Conclusions

---

[1] In order to test whether the difference patterns shown in section 5 are statistically robust we also use the statistics averaged over an ENSO event as our sample points to perform two-tailed tests. Figs. S3–S9 shown in the supplement demonstrate that those difference patterns are statistically significant at the 5% significance level to a large extent.

787   Both Kawatani et al. (2019) and Serva et al. (2020) pointed out that a relatively high horizontal

788   resolution is necessary to simulate the ENSO modulation of the QBO period. Employing an Earth system

789   model with T42 (~2.79°) horizontal resolution, Kawatani et al. (2019) further demonstrated that the

790   ENSO modulation of the QBO could not be simulated with their fixed GW sources. Serva et al. (2020)

791   also pointed out that the reliance on stationary parameterizations of GWs is partly responsible for failing

792   to simulate the observed modulation of the QBO by the ENSO in current climate models.

793   Rind et al. (1988) implemented various interactive GW sources in the GISS climate models. With the

794   momentum flux of the parameterized convective waves dependent on the convective mass flux,

795   buoyancy frequency and density at the top of the convective region, wind velocity averaged over the

796   convective layers, etc. and with a horizontal resolution of 2° latitude by 2.5° longitude, all the four

797   versions of GISS E2.2 models in this study can simulate the ENSO modulation of the QBO period to

798   various degrees. For each of 19 runs conducted in this study, the absolute momentum fluxes at the source

799   levels over the equatorial belt is larger during El Niño episodes than during La Niña episodes, leading

800   to a shorter and longer QBO period, respectively.

801   Realistic simulation of the ENSO modulation of the QBO periods entails the realistic simulation of

802   both the ENSO and the QBO. With the realistic SSTs specified, both the composite difference in the

803   Walker circulation and the composite OLR difference between warm and cold ENSO extremes simulated

804   by the two AMIP E2.2 models are close to the observed. Since the AMIP model with the "altered physics"

805   performs better than that with the "standard physics" as far as the simulated OLR is concerned, the

806   ensemble mean difference in the QBO period between La Niña and El Niño episodes (i.e., ~4.5 months)

807   simulated by AMIP–OMA–AP is larger than that simulated by AMIP–OMA–SP (i.e., ~3.9 months),

808   which indicates that convective parameterization scheme is important not only for simulating the

809   resolved waves as pointed out by Horinouchi et al. (2003) and Lott et al. (2014), but also for

810   parameterizing GWs. However, the convective activities simulated by both AMIP E2.2 models are still

811   inadequate over the central and eastern equatorial Pacific as compared to the observed, which may partly

812   account for why the ensemble mean differences in the QBO period between La Niña and El Niño

813   episodes simulated by both AMIP models are smaller than the observed difference (i.e., ~8.7 months).

814   Although the simulated Walker circulation associated with the ENSO cycle is comparable among the

815   two coupled ocean-atmosphere models in this study, the E2.2 model with the "standard physics"

816   performs well in its simulated SSTs which is very close to the observed while the ENSO amplitudes

817   simulated by the other model with the "altered physics" are substantially greater than the observed. Yet

818   the model with the "standard physics" not only fails to properly simulate the shift of the strongest

819   convection from the maritime continent during La Niña to the central and eastern equatorial Pacific

820   during El Niño, but also grossly fail to simulate the sufficient amplitude of the OLR concomitant with

821   the ENSO cycle. The weaker response of the Walker circulation and convective activities to the ENSO

822   cycle together with the dislocated centers of convection concomitant to cold and warm ENSO extremes

823   leads to the smallest ensemble mean difference in the QBO period between La Niña and El Niño episodes

824   (i.e., ~2.7 months) simulated by the Coupled–NINT–SP model. The weaker variation of the Walker

825   circulation and the excessive change in convection compensate to give an impression of realistically

826   simulating the ENSO modulation of the QBO period by the other model with the "altered physics", i.e.,

827   Coupled–NINT–AP, with its ensemble mean differences in the QBO period between La Niña and El

828   Niño episodes being ~4.8 months. However, it is worth pointing out that we don't regard that model as

829   the best among the four models listed in Table 1 because the relatively satisfactory results are achieved

830   in a compensatory, thus unrealistic, way. Serva et al. (2020) conducted both the atmosphere-only and

831   coupled historical simulations and found that the trough-to-crest amplitudes of the OLR associated with

832   the ENSO cycle are two times larger than the observed for a few models that relatively well capture the

ENSO modulation of the QBO period, which together with our results suggests that the parameterized

convection is a linchpin of realistically simulating the ENSO, the QBO, and the ENSO modulation of

the QBO.

Intriguingly, the simulated difference in the QBO period between La Niña and El Niño is 6.2 months

from the first realization simulated by Coupled–NINT–SP. However, it is not statistically significant at

the 5% significance level. Meanwhile, the differences in the QBO period between La Niña and El Niño

from most of the realizations simulated by Coupled–NINT–AP are apparently less than 6.2 months but

are all statistically significant. To gain a deeper insight, we calculate the frequency power spectra of

standardized ONIs derived from the observed and simulated SSTs. Fig. 13a depicts the power spectral

densities (PSD) of standardized ONI between 1953 and 2015 derived from the NOAA ERSSTv5 SST

while Fig. 13b delineates the PSD of standardized ONI between 1871 and 2013 derived from the

HadISST1 dataset as used in the AMIP runs. Figs. 13a and 13b show that although the ENSO accounts

for the lion's share of SST variabilities, there is a good amount of SST variabilities on the decadal and

multidecadal time scales. Fig. 13d illustrates the PSD of standardized ONI between 1871 and 2013

simulated by the second realization of Coupled–NINT–AP, which demonstrates that the ENSO

overwhelmingly dominates over any other noises in SST variabilities simulated by those E2.2 models

with the "altered physics". Furthermore, Fig. 13c shows the PSD of standardized ONI between 1871 and

2013 simulated by the first realization of Coupled–NINT–SP. Apparently, the SST variabilities

simulated by the E2.2 model with the "standard physics" are comparable to the observed, thus more

realistic. The smaller ratio of the ENSO signal to the noise simulated by the first realization of Coupled–

NINT–SP and the much larger ratio simulated by the second realizations of the E2.2 models with "alter

physics" explain why the difference of 6.2 months in the QBO period between La Niña and El Niño

855   from the former is not statistically significant while the differences of 2.6 and 4.8 months from the latter

856   are statistically significant as shown in Table 2.

857   The rich spectrum of internal variabilities simulated by Coupled–NINT–SP, to a large degree, reflects

858   the observed ones shown in Figs. 13a and13b. Those large internal variabilities likely underlie why one

859   of the historical runs simulated by Coupled–NINT–SP gives rise to a slower mean QBO phase speed

860   during El Niño than during La Niña while other four runs from Coupled–NINT–SP do simulate a faster

861   phase speed of the QBO during warm ENSO events. Kawatani et al. (2019) conducted two 100-yr

862   experiments: one for a perpetual El Niño condition and the other for a perpetual La Niña condition. Their

863   Fig. 3 shows that although the long-term mean QBO period from the El Niño run is shorter than that

864   from the La Niña run, this is not the case for each individual year. This is because various internal

865   variabilities exert their influence over the QBO period.

866   None of the E2.2 configurations robustly simulate an ENSO modulation of QBO amplitude,

867   consistent with the weaker signal present in observations (Yuan et al., 2014). It is not surprising because

868   our observational analyses show that the ENSO modulation of the QBO amplitude is not statistically

869   significant at the 95% confidence level. In order to realistically simulate the ENSO modulation of the

870   QBO, various aspects of climate models such as the SSTs, the Walker circulation, the parameterizations

871   of convection and GWs need to be further improved, which is fortunately ongoing under the auspices of

872   the SPARC Quasi-Biennial Oscillation initiative (Butchart et al., 2018).

873

874   **Data availability**

875   The monthly mean zonal winds from Free University of Berlin are obtained from https://www.geo.fu-

876   berlin.de/en/met/ag/strat/produkte/qbo/index.html. The NOAA ERSSTv5 SST is acquired from

877   https://www.ncei.noaa.gov/products/extended-reconstructed-sst. The NCEI OLR is downloaded from

878 https://www.ncei.noaa.gov/products/climate-data-records/outgoing-longwave-radiation-monthly. The

879 ERA5 monthly mean zonal winds are obtained from the ECMWF C3S at Climate Data Store:

880 https://cds.climate.copernicus.eu/. The Coupled–NINT–AP outputs are available from the Earth System

881 Grid Federation. The data used in this paper from the other three E2.2 models are accessible at

882 https://zenodo.org/record/8360291.

883

884 **Supplementary Figures**

885 Figs. S1–S5 are supplementary to Figs. 2–6, respectively.

886 Fig. S6 are supplementary to Fig. 8.

887 Figs. S7–S9 are supplementary to Figs. 10–12, respectively.

888

889 **Author contributions**

890 All authors made equal contributions to this work.

891

892 **Competing interests**

893 The authors declare that they have no conflict of interest.

894

895 **Acknowledgements:** Climate modeling at GISS is supported by the NASA Modeling, Analysis and

896 Prediction program, and resources supporting this work were provided by the NASA High-End

897 Computing (HEC) Program through the NASA Center for Climate Simulation (NCCS) at Goddard Space

898 Flight Center. The authors thank three anonymous reviewers for their constructive comments, which led

899 to a significantly improved paper.

900

References

Alexander, M. J., Ortland, D. A., Grimsdell, A. W., and Kim, J.-E.: Sensitivity of Gravity Wave Fluxes to Interannual Variations in Tropical Convection and Zonal Wind, J. Atmos. Sci., 74, 2701–2716, https://doi.org/10.1175/JAS-D-17-0044.1, 2017.

Andrews, D. G., Mahlman, J. D., and Sinclair, R. W.: Eliassen–Palm diagnostics of wave-mean flow interaction in the GFDL" SKYHI" general circulation model, J. Atmos. Sci., 40, 2768–2784, https://doi.org/10.1175/1520-0469(1983)040%3C2768:ETWATM%3E2.0.CO;2, 1983.

Andrews, D. G., Holton, J. R., and Leovy, C. B.: Middle Atmosphere Dynamics, Academic Press, 489 pp, 1987.

Angell, J. K.: On the variation in period and amplitude of the quasi-biennial oscillation in the equatorial stratosphere, 1951–85, Mon. Weather Rev., 114, 2272–2278, https://doi.org/10.1175/1520-0493(1986)114%3C2272:OTVIPA%3E2.0.CO;2, 1986.

Anstey, J. A., Banyard, T. P., Butchart, N., Coy, L., Newman, P. A., Osprey, S., and Wright, C. J.: Prospect of Increased Disruption to the QBO in a Changing Climate, Geophys. Res. Lett., 48, e2021GL093058, https://doi.org/10.1029/2021GL093058, 2021.

Baldwin, M. P., Gray, L. J., Dunkerton, T. J., Hamilton, K., Haynes, P. H., Randel, W. J., Holton, J. R., Alexander, M. J., Hirota, I., Horinouchi, T., Jones, D. B. A., Kinnersley, J. S., Marquardt, C., Sato, K., and Takahashi, M.: The Quasi-biennial oscillation, Rev. Geophys., 39, 179–229, https://doi.org/10.1029/1999RG000073, 2001.

Bauer, S. E., Tsigaridis, K., Faluvegi, G., Kelley, M., Lo, K. K., Miller, R. L., Nazarenko, L., Schmidt, G. A., and Wu, J.: Historical (1850–2014) Aerosol Evolution and Role on Climate Forcing Using the GISS ModelE2.1 Contribution to CMIP6, J. Adv. Model. Earth Sy., 12, e2019MS001978, https://doi.org/10.1029/2019ms001978, 2020.

924 Bergman, J. W. and Salby, M. L.: Equatorial wave activity derived from fluctuations in observed

925   convection, J. Atmos. Sci. 51, 3791–3806, https://doi.org/10.1175/1520-

926   0469(1994)051%3C3791:EWADFF%3E2.0.CO;2, 1994.

927 Bjerknes, J.: Atmospheric teleconnections from the equatorial Pacific, Mon. Weather Rev., 97, 163–172,

928   https://doi.org/10.1175/1520-0493(1969)097%3C0163:ATFTEP%3E2.3.CO;2, 1969.

929 Bushell, A. C., Anstey, J. A., Butchart, N., Kawatani, Y., Osprey, S. M., Richter, J. H., Serva, F.,

930   Braesicke, P., Cagnazzo, C., Chen, C.-C., Chun, H.-Y., Garcia, R. R., Gray, L. J., Hamilton, K.,

931   Kerzenmacher, T., Kim, Y.-H., Lott, F., McLandress, C., Naoe, H., Scinocca, J., Smith, A. K.,

932   Stockdale, T. N., Versick, S., Watanabe, S., Yoshida, K., and Yukimoto, S.: Evaluation of the Quasi-

933   Biennial Oscillation in global climate models for the SPARC QBO-initiative, Q. J. Roy. Meteor.

934   Soc., 1–31, https://doi.org/10.1002/qj.3765, 2020.

935 Butchart, N., Anstey, J., Hamilton, K., Osprey, S., McLandress, C., Bushell, A. C., Kawatani, Y., Kim,

936   Y.-H., Lott, F., Scinocca, J., Stockdale, T.N., Andrews, M., Bellprat, O., Braesicke, P., Cagnazzo,

937   C., Chen, C.-C., Chun, H.-Y., Dobrynin, M., Garcia, R., Garcia-Serrano, J., Gray, L.J., Holt, L.,

938   Kerzenmacher, T., Naoe, H., Pohlmann, H., Richter, J. H., Scaife, A.A., Schenzinger, V., Serva, F.,

939   Versick, S., Watanabe, S., Yoshida, K. and Yukimoto, S.: Overview of experiment design and

940   comparison of models participating in phase 1 of the SPARC Quasi-Biennial Oscillation initiative

941   (QBOi), Geoscientific Model Development, 11, 1009–1032. https://doi.org/10.5194/gmd-11-1009-

942   2018, 2018.

943 Calvo, N., Garcia, R. R., Randel, W. J., and Marsh, D. R.: Dynamical mechanism for the increase in

944   tropical upwelling in the lowermost tropical stratosphere during warm ENSO events, J. Atmos. Sci.,

945   67, 2331–2340, https://doi.org/10.1175/2010JAS3433.1, 2010.

Cane, M. and Zebiak, S. E.: Prediction of El Niño events using a physical model, in Atmospheric and Oceanic Variability, edited by H. Cattle, Royal Meteorological Society Press, London, 153-182, 1987.

Chernick, M. R.: Bootstrap methods: A guide for practitioners and researchers, Wiley-Interscience, 369pp, 2007).

Christiansen, B., Yang, S., and Madsen, M. S.: Do strong warm ENSO events control the phase of the stratospheric QBO?, Geophys. Res. Lett., 43, 10489–10495, https://doi.org/10.1002/2016GL070751, 2016.

Collimore, C. C., Martin, D. W., Hitchman, M. H., Huesmann, A., and Waliser, D. E.: On the relationship between the QBO and tropical deep convection, J. Climate, 16, 2552–2568, https://doi.org/10.1175/1520-0442(2003)016%3C2552:OTRBTQ%3E2.0.CO;2, 2003.

Coy, L., Newman, P. A., Strahan, S., and Pawson, S.: Seasonal variation of the quasi-biennial oscillation descent, J. Geophys. Res.-Atmos., 125, e2020JD033077, https://doi.org/10.1029/2020JD033077, 2020.

DallaSanta, K., Orbe, C., Rind, D., Nazarenko, L., and Jonas, J.: Dynamical and trace gas responses of the Quasi-Biennial Oscillation to increased CO_2, J. Geophys. Res. Atmos., 126, e2020JD034151. https://doi.org/10.1029/2020JD034151, 2021.

Domeisen, D. I. V., Garfinkel, C. I., and Butler, A. H.: The Teleconnection of El Niño Southern Oscillation to the Stratosphere, Rev. Geophys., 57, 5–47, https://doi.org/10.1029/2018RG000596, 2019.

Garfinkel, C. I. and Hartmann, D. L.: Effects of El Nino – South- ern Oscillation and the Quasi-Biennial Oscillation on polar tem- peratures in the stratosphere, J. Geophys. Res., 112, D19112, https://doi.org/10.1029/2007JD008481, 2007.

Garfinkel, C. I. and Hartmann, D. L.: The influence of the quasi-biennial oscillation on the troposphere in winter in a hierarchy of models. Part I: Simplified dry GCMs, J. Atmos. Sci., 68, 1273–1289, https://doi.org/10.1175%2F2011JAS3665.1, 2011a.

Garfinkel, C. I. and Hartmann, D. L.: The influence of the quasi-biennial oscillation on the troposphere in winter in a hierarchy of models. Part II: Perpetual winter WACCM runs, J. Atmos. Sci., 68, 2026–2041, https://doi.org/10.1175%2F2011JAS3702.1, 2011b.

Geller, M. A., Zhou, T., Shindell, D., Ruedy, R., Aleinov, I., Nazarenko, L., Tausnev, N. L., Kelley, M., Sun, S., Cheng, Y., Field, R. D., and Faluvegi, G.: Modeling the QBO-improvements resulting from higher-model vertical resolution, J. Adv. Model. Earth Syst., 8, 1092–1105, https://doi.org/10.1002/2016MS000699, 2016a.

Geller, M. A., Zhou, T., and Yuan, W.: The QBO, gravity waves forced by tropical convection, and ENSO, J. Geophys. Res. Atmos., 121, 8886-8895, https://doi.org/10.1002/2015JD024125, 2016b.

Giorgetta, M. A., Bengtson, L., and Arpe, K.: An investigation of QBO signals in the east Asian and Indian monsoon in GCM experiments, Climate Dynamics, 15, 435–450, https://doi.org/10.1007/s003820050292, 1999.

Giorgetta, M. A., Manzini, E., and Roeckner, E., Esch, M., and Bengtsson, L.: Climatology and forcing of the quasi-biennial oscillation in the MAECHEM5 model, J. Climate, 19, 3882–3901, https://doi.org/10.1175/JCLI3830.1, 2006.

Graham, N. E. and Barnett, T. P.: Sea surface temperature, surface wind divergence, and convection over tropical oceans, Science, 238, 657–659, https://doi.org/10.1126/science.238.4827.657, 1987.

Gray, W. M.: Atlantic seasonal hurricane frequency. Part I: El Niño and 30-mb quasi-biennial oscillation influences, Mon. Wea. Rev., 112, 1649–1688, https://doi.org/10.1175/1520-0493(1984)112%3C1649:ASHFPI%3E2.0.CO;2, 1984.

Gray, W. M., Sheaffer, J. D., and Knaff, J.: Influence of the stratospheric QBO on ENSO variability, J. Meteor. Soc. Jpn., 70, 975–995, https://doi.org/10.2151/jmsj1965.70.5_975, 1992.

Grothe, P. R., Cobb, K. M., Liguori, G., Di Lorenzo, E., Capotondi, A., Lu, Y., Cheng, H., Edwards, R.L., Southon, J. R., Santos, G. M., Deocampo, D. M., Lynch-Stieglitz, J., Chen, T., Sayani, H. R., Thompson, D. M., Conroy, J. L., Moore, A. L., Townsend, K., Hagos, M., O'Connor, G., and Toth, L. T.: Enhanced El Niño–Southern oscillation variability in recent decades, Geophys. Res. Lett., 47, e2019GL083906, https://doi.org/10.1029/2019GL083906, 2019.

Hamilton, K., Osprey, S., and Butchart, N.: Modeling the stratosphere's "heartbeat," Eos, 96, p. 8, https://doi.org/10.1029/2015EO032301, 2015.

Hamilton, K., Hertzog, A., Vial, F., and Stenchikov, G.: Longitudinal variation of the stratospheric Quasi-Biennial Oscillation, J. Atmos. Sci., 61, 383–402, https://doi.org/10.1175/1520-0469(2004)061%3C0383:LVOTSQ%3E2.0.CO;2, 2004.

Hansen, F., Matthes, K., and Wahl, S.: Tropospheric QBO–ENSO interactions and differences between the Atlantic and Pacific, J. Climate, 29, 1353–1368, https://doi.org/10.1175/JCLI-D-15-0164.1, 2016

Hasebe, F.: Quasi-biennial oscillations of ozone and diabatic circulation in the equatorial stratosphere, J. Atmos. Sci., 51, 729–745, https://doi.org/10.1175/1520-0469(1994)051%3c0729:QBOOOA%3e2.0.CO;2, 1994.

Haynes, P. H., McIntyre, M. E., Shepherd, T. G., Marks, C. J., and Shine, K. P.: On the "Downward Control" of Extratropical Diabatic Circulations by Eddy-Induced Mean Zonal Forces, J. Atmos. Sci., 48, 651–678, https://doi.org/10.1175/1520-0469(1991)048%3C0651:OTCOED%3E2.0.CO;2, 1991.

Hersbach, H., Bell, B., Berrisford, P., Hirahara, S., Horányi, A., Muñoz-Sabater, J., Nicolas, J., Peubey, C., Radu, R., Schepers, D., Simmons, A., Soci, C., Abdalla, S., Abellan, X., Balsamo, G., Bechtold,

1015   P., Biavati, G., Bidlot, J., Bonavita, M., Chiara, G., Dahlgren, P., Dee, D., Diamantakis, M., Dragani,

1016   R., Flemming, J., Forbes, R., Fuentes, M., Geer, A., Haimberger, L., Healy, S., Hogan, R. J., Hólm,

1017   E., Janisková, M., Keeley, S., Laloyaux, P., Lopez, P., Lupu, C., Radnoti, G., Rosnay, P., Rozum, I.,

1018   Vamborg, F., Villaume, S., and Thépaut, J.-N.: The ERA5 global reanalysis, Q. J. Roy. Meteor. Soc.,

1019   online first, https://doi.org/10.1002/qj.3803, 2020.

1020   Hitchman, M. H., and Huesmann, A. S.: Seasonal influence of the quasi-biennial oscillation on

1021   stratospheric jets and Rossby wave breaking, J. Atmos. Sci., 66, 935–946,

1022   https://doi.org/10.1175%2F2008JAS2631.1, 2009.

1023   Ho, C.-H., Kim, H.-S., Jeong, J.-H., and Son, S.-W.: Influence of stratospheric quasi-biennial oscillation

1024   on tropical cyclone tracks in the western North Pacific, Geophys. Res. Lett., 36, L06702,

1025   http://dx.doi.org/10.1029/2009GL037163, 2009.

1026   Holton, J.: Waves in the equatorial stratospheric generated by tropospheric heat resources, J. Atmos. Sci.,

1027   27, 368–375, https://doi.org/10.1175/1520-0469(1972)029%3C0368:WITESG%3E2.0.CO;2, 1972.

1028   Holton, J. R. and Lindzen, R. S.: An updated theory for the quasi-biennial cycle of the tropical

1029   stratosphere, J. Atmos. Sci., 29, 1076–1080, https://doi.org/10.1175/1520-

1030   0469(1972)029%3c1076:AUTFTQ%3e2.0.CO;2, 1972.

1031   Holton, J. R. and Tan, H.: The Influence of the equatorial quasi-biennial oscillation on the global

1032   circulation at 50 mb, J. Atmos. Sci., 37, 2200–2208, https://doi.org/10.1175/1520-

1033   0469(1980)037%3c2200:TIOTEQ%3e2.0.CO;2, 1980.

1034   Horinouchi, T., Pawson, S., Shibata, K., Manzini, E., Giorgetta, M., and Sassi, F.: Tropical cumulus

1035   convection and upward propagating waves in middle-atmospheric GCMs, J. Atmos. Sci., 60, 2765–

1036   2782, https://doi.org/10.1175/1520-0469(2003)060%3C2765:TCCAUW%3E2.0.CO;2, 2003.

1037 Hu, Z.-Z., Huang, B., Kinter, J. L., Wu, Z., and Kumar, A.: Connection of the stratospheric QBO with

1038   global atmospheric general circulation and tropical SST. Part II: Interdecadal variations, Climate

1039   Dynamics, 38, 25–43, https://doi.org/10.1007/s00382-011-1073-6, 2012.

1040 Huang, B. H., Hu, Z. Z., Kinter, J. L., Wu, Z. H., and Kumar, A.: Connection of stratospheric QBO with

1041   global atmospheric general circulation and tropical SST. Part I: Methodology and composite life

1042   cycle, Climate Dynamics, 38, 1–23, https://doi.org/10.1007%2Fs00382-011-1250-7, 2012.

1043 Huang, B., Thorne, P. W., Banzon, V. F., Boyer, T., Chepurin, G., Lawrimore, J. H., Menne M. J., Smith,

1044   T. M., Vose R. S., and Zhang, H. M.: Extended reconstructed sea surface temperature, version 5

1045   (ERSSTv5): upgrades, validations, and intercomparisons, J. Climate, 30, 8179–

1046   8205, https://doi.org/10.1175/JCLI-D-16-0836.1, 2017.

1047 Kang, M.-J., Chun, H.-Y., Kim, Y.-H., Preusse, P., and Ern, M.: Momentum flux of convective gravity

1048   waves derived from an offline gravity wave parameterization. Part II: Impacts on the Quasi-Biennial

1049   Oscillation, J. Atmos. Sci., 75, 3753–3775, https://doi.org/10.1175/JAS-D-18-0094.1, 2018.

1050 Kawatani, Y, Lee, J. N., and Hamilton, K.: Interannual variations of stratospheric water vapor in MLS

1051   observations and climate model simulations, J. Atmos. Sci., 71, 4072–4085,

1052   https://doi.org/10.1175/JAS-D-14-0164.1, 2014.

1053 Kawatani, Y., Hamilton, K., Sato, K., Dunkerton, T. J., Watanabe, S., and Kikuchi, K.: ENSO Modulation

1054   of the QBO: Results from MIROC Models with and without Nonorographic Gravity Wave

1055   Parameterization, J. Atmos. Sci., 76, 3893–3917, https://doi.org/10.1175/JAS-D-19-0163.1, 2019.

1056 Kelley, M., Schmidt, G. A., Nazarenko, L. S., Bauer, S. E., Ruedy, R., Russell, G. L., Ackerman, A. S.,

1057   Aleinov, I., Bauer, M., Bleck, R., Canuto, V., Cesana, G., Cheng, Y., Clune, T. L., Cook, B. I., Cruz,

1058   C. A., Del Genio, A. D., Elsaesser, G. S., Faluvegi, G., Kiang, N. Y., Kim, D., Lacis, A. A.,

1059   Leboissetier, A., LeGrande, A. N., Lo, K. K., Marshall, J., Matthews, E. E., McDermid, S., Mezuman,

1060   K., Miller, R. L., Murray, L. T., Oinas, V., Orbe, C., Pérez, C., García-Pando, C., Perlwitz, J. P.,

1061   Puma, M. J., Rind, D., Romanou, A., Shindell, D. T., Sun, S., Tausnev, N., Tsigaridis, K., Tselioudis,

1062   G., Weng, E., Wu, J., and Yao, M.-S.: GISS-E2.1: Configurations and climatology, J. Adv. Model.

1063   Earth Sy., 12, e2019MS002025, https://doi.org/10.1029/2019MS002025, 2020.

1064 Kumar V., Yoden, S., and Hitchman, M. H.: QBO and ENSO effects on the mean meridional circulation,

1065   polar vortex, subtropical westerly jets, and wave patterns during boreal winter, *J. Geophys. Res.* 127,

1066   e2022JD036691, https://doi.org/10.1029/2022JD036691, 2022.

1067 Labitzke, K.: On the interannual variability of the middle stratosphere during the northern winters, J.

1068   Meteorol. Soc. Jpn., 80, 963–971, http://doi.org/10.2151/jmsj1965.60.1_124, 1982.

1069 Liess, S. and Geller, M. A.: On the relationship between QBO and distribution of tropical deep

1070   convection, J. Geophys. Res., 117, D03108, http://dx.doi.org/10.1029/2011JD016317, 2012.

1071 Lindzen, R. S. and Holton, J. R.:   A theory of the quasi-biennial oscillation, J. Atmos. Sci., 25, 1095–

1072   1107, https://doi.org/10.1175/1520-0469(1968)025%3C1095:ATOTQB%3E2.0.CO;2, 1968.

1073 Lott, F., Denvil, S., Butchart, N., Cagnazzo, C., Giorgetta, M. A., Hardiman, S. C., Manzini, E.,

1074   Krismer, T., Duvel, J.-P., Maury, P., Scinocca, J. F., Watanabe, S., and Yukimoto, S.: Kelvin

1075   and Rossby-gravity wave packets in the lower stratosphere of some high-top CMIP5 models, J.

1076   Geophys. Res., 119, 2156–2173, https://doi.org/10.1002/2013JD020797, 2014.

1077 Maruyama, T. and Tsuneoka, Y.: Anomalously short duration of the QBO at 50 hPa of the easterly wind

1078   phase in 1987 and its relationship to an El Niño event, J. Meteorol. Soc. Jpn., 66, 629–634,

1079   https://doi.org/10.2151/jmsj1965.66.4_629, 1988.

1080 Miller, R. L., Schmidt, G. A., Nazarenko, L. S., Bauer, S. E., Kelley, M., Ruedy, R., Russell, G. L.,

1081   Ackerman, A. S., Aleinov, I., Bauer, M., Bleck, R., Canuto, V., Cesana, G., Cheng, Y., Clune, T. L.,

1082   Cook, B. I., Cruz, C. A., Del Genio, A. D., Elsaesser, G. S., Faluvegi, G., Kiang, N. Y., Kim, D.,

1083   Lacis, A. A., Leboissetier, A., LeGrande, A. N., Lo, K. K., Marshall, J., Matthews, E. E., McDermid,

1084   S., Mezuman, K., Murray, L. T., Oinas, V., Orbe, C., Pérez García-Pando, C., Perlwitz, J. P., Puma,

1085   M. J., Rind, D., Romanou, A., Shindell, D. T., Sun, S., Tausnev, N., Tsigaridis, K., Tselioudis, G.,

1086   Weng, E., Wu, J., and Yao, M. S.: CMIP6 Historical Simulations (1850–2014) With GISS-E2.1, J.

1087   Adv. Model. Earth Syst., 13, e2019MS002034, https://doi.org/10.1029/2019MS002034, 2021.

1088 Moser, B. K. and Stevens, G. R.: Homogeneity of variance in the two-sample means test, Am. Stat., 46,

1089   19–21, https://doi.org/10.1080/00031305.1992.10475839, 1992.

1090 Naujokat, B.: An update of the observed quasi–biennial oscillation of the stratospheric winds over the

1091   tropics, J. Atmos. Sci., 43, 1873–1877, https://doi.org/10.1175/1520-

1092   0469(1986)043%3C1873:AUOTOQ%3E2.0.CO;2, 1986.

1093 Nazarenko, L. S., Tausnev, N., Russell, G. L., Rind, D., Miller, R. L., Schmidt, G. A., Bauer, S. E., Kelley,

1094   M., Ruedy, R., Ackerman, A. S., Aleinov, I., Bauer, M., Bleck, R., Canuto, V., Cesana, G., Cheng,

1095   Y., Clune, T. L., Cook, B. I., Cruz, C. A., Del Genio, A. D., Elsaesser, G. S., Faluvegi, G., Kiang, N.

1096   Y., Kim, D., Lacis, A. A., Leboissetier, A., LeGrande, A. N., Lo, K. K., Marshall, J., Matthews, E.

1097   E., McDermid, S., Mezuman, K., Murray, L. T., Oinas, V., Orbe, C., Pérez García-Pando, C.,

1098   Perlwitz, J. P., Puma, M. J., Romanou, A., Shindell, D. T., Sun, S., Tsigaridis, K., Tselioudis, G.,

1099   Weng, E., Wu, J., and Yao, M.-S.: Future Climate Change Under SSP Emission Scenarios With

1100   GISS-E2.1, J. Adv. Model. Earth Syst., 14,

1101   e2021MS002871, https://doi.org/10.1029/2021MS002871, 2022.

1102 Oort, A. H. and Yienger, J. J.: Observed interannual variability in the Hadley circulation and its

1103   connection to ENSO, J. Climate, 9, 2751–2767, https://doi.org/10.1175/1520-

1104   0442(1996)009<2751:Oivith>2.0.Co;2, 1996.

1105   Orbe, C., Rind, D., Jonas, J., Nazarenko, L., Faluvegi, G., Murray, L.T., Shindell, D.T., Tsigaridis, K.,

1106   Zhou, T., Kelley, M., and Schmidt, G.: GISS Model E2.2: A climate model optimized for the middle

1107   atmosphere. Part 2: Validation of large-scale transport and evaluation of climate response, *J.*

1108   *Geophys. Res. Atmos.*, 125, e2020JD033151, https://doi.org/10.1029/2020JD033151, 2020.

1109   Philander, S. G. H.: El Niño, La Niña, and the Southern Oscillation, Academic Press, San Diego, 293pp.,

1110   1990.

1111   Plumb, R. A.: The interaction of two internal waves with the mean flow: Implications for the theory of

1112   the quasi-biennial oscillation, J. Atmos. Sci., 34, 1847–1858, https://doi.org/10.1175/1520-

1113   0469(1977)034<1847:TIOTIW>2.0.CO;2, 1977.

1114   Rao, J., Garfinkel, C. I., and White, I. P.: Impact of the Quasi-Biennial Oscillation on the Northern Winter

1115   Stratospheric   Polar   Vortex   in   CMIP5/6   Models,   J.   Climate,   33,   4787–

1116   4813, https://doi.org/10.1175/JCLI-D-19-0663.1, 2020a.

1117   Rao, J., Garfinkel, C. I., and White, I. P.: Projected strengthening of the extratropical surface impacts of

1118   the   stratospheric   quasi-biennial   oscillation,   Geophys.   Res.   Lett.,   47,

1119   e2020GL089149, https://doi.org/10.1029/2020GL089149, 2020b.

1120   Rao, J., Garfinkel, C. I., and White, I. P.: Development of the Extratropical Response to the Stratospheric

1121   Quasi-Biennial Oscillation, J. Climate, 34, 7239–7255, https://doi.org/10.1175/JCLI-D-20-0960.1

1122   2021.

1123   Rao, J., Garfinkel, C. I., White, I. P., and Schwartz, C.: How does the Quasi-Biennial Oscillation affect the

1124   boreal   winter   tropospheric   circulation   in   CMIP5/6   models?,   J.   Climate,   33,   8975–8996,

1125   https://doi.org/10.1175/JCLI-D-20-0024.1, 2020c.

1126   Rayner, N. A., Parker, D. E., Horton, E. B., Folland, C. K., Alexander, L. V., Rowell, D. P., Kent, E. C.,

1127   and Kaplan, A.: Global analyses of sea surface temperature, sea ice, and night marine air temperature

1128   since   the   late   nineteenth   century,   J.   Geophys.   Res.,   108,   4407,

1129   https://doi.org/10.1029/2002JD002670, 2003.

1130   Richter, J. H., Solomon, A., and Bacmeister, J. T.: On the simulation of the quasi-biennial oscillation in

1131   the Community Atmosphere Model, version 5, J. Geophys. Res.-Atmos., 119, 3045–

1132   3062, https://doi.org/10.1002/2013JD021122, 2014.

1133   Richter, J. H., Anstey, J. A., Butchart, N., Kawatani, Y., Meehl, G. A., Osprey, S., and Simpson, I. R.:

1134   Progress in simulating the quasi-biennial oscillation in CMIP models, J. Geophys. Res.-Atmos., 125,

1135   e2019JD032362, https://doi.org/10.1029/2019JD032362, 2020.

1136   Rind, D., Lerner, J., Jonas, J., and McLinden, C.: Effects of resolution and model physics on tracer

1137   transports in the NASA Goddard Institute for Space Studies general circulation models, J. Geophys.

1138   Res., 112, D09315, https://doi.org/10.1029/2006JD007476, 2007.

1139   Rind, D., Suozzo, R., Balachandran, N. K., Lacis, A., and Russell, G.: The GISS global climate-middle

1140   atmosphere model. Part I: Model structure and climatology, J. Atmos. Sci., 45, 329–370,

1141   https://doi.org/10.1175/1520-0469(1988)045%3C0329:TGGCMA%3E2.0.CO;2, 1988.

1142   Rind, D., Jonas, J., Balachandran, N., Schmidt, G., and Lean, J.: The QBO in two GISS global climate

1143   models: 1.   Generation   of   the   QBO,   J.   Geophys.   Res.   Atmos.,   119,   8798–8824,

1144   https://doi.org/10.1002/2014JD021678, 2014.

1145   Rind, D., Orbe, C., Jonas, J., Nazarenko, L., Zhou, T., Kelley, M., Lacis, A., Shindell, D., Faluvegi,

1146   Russell, G., Bauer, M., Schmidt, G., Romanou, A., and Tausnev, N.: GISS Model E2.2: A climate

1147   model optimized for the middle atmosphere — Model structure, climatology, variability and climate

1148   sensitivity, J. Geophys. Res. Atmos., 125, e2019JD032204, https://doi.org/10.1029/2019JD032204,

1149   2020.

1150   Salby, M. L.: Physics of the Atmosphere and Climate, Cambridge University Press, New York,

1151   https://doi.org/10.1017/CBO9781139005265, 2012.

1152   Salby, M. L. and Garcia, R. R.: Transient response to localized episodic heating in the tropics, Part 1:

1153   excitation and short-time near-field behavior, J. Atmos. Sci., 44, 458–498,

1154   https://doi.org/10.1175/1520-0469(1987)044%3C0458:TRTLEH%3E2.0.CO;2, 1987.

1155   Sarachik, E. S. and Cane, M. A.: The El Niño-Southern Oscillation Phenomenon, Cambridge University

1156   Press, Cambridge, 364pp., 2010.

1157   Scaife, A. A., Butchart, N., Warner, C. D., Stainforth, D., Norton, W., and Austin, J.: Realistic quasi-

1158   biennial oscillations in a simulation of the global climate, Geophys. Res. Lett., 27, 3481–3484,

1159   https://doi.org/10.1029/2000GL011625, 2000.

1160   Schirber, S., Manzini, E., Krismer, T. and Giorgetta, M.: The Quasi-Biennial Oscillation in a warmer

1161   climate: sensitivity to different gravity wave parameterizations, Climate Dynamics, 45, 825–

1162   836, https://doi.org/10.1007/s00382-014-2314-2, 2015.

1163   Schmidt, G. A., Kelley, M., Nazarenko, L., Ruedy, R., Russell, G. L., Aleinov, I., Bauer, M., Bauer, S.

1164   E., Bhat, M. K., Bleck, R., Canuto, V., Chen, Y.-H., Cheng, Y., Clune, T. L., Del Genio, A., de

1165   Fainchtein, R., Faluvegi, G., Hansen, J. E., Healy, R. J., Kiang, N. Y., Koch, D., Lacis, A. A.,

1166   LeGrande, A. N., Lerner, J., Lo, K. K., Matthews, E. E., Menon, S., Miller, R. L., Oinas, V.,

1167   Oloso, A. O., Perlwitz, J. P., Puma, M. J., Putman, W. M., Rind, D., Romanou, A., Sato, M.,

1168   Shindell, D. T., Sun, S., Syed, R. A., Tausnev, N., Tsigaridis, K., Unger, N., Voulgarakis, A.,

1169   Yao, M.-S., and Zhang, J.: Configuration and assessment of the GISS ModelE2 contributions to

1170   the CMIP5 archive, J. Adv. Model. Earth Syst., 6, 141–

1171   184, https://doi.org/10.1002/2013MS000265, 2014.

Scott, R. K. and Haynes, P. H.: Internal interannual variability of the extratropical stratospheric circulation: The low-latitude flywheel, Q. J. Roy. Meteor. Soc., 124, 2149–2173, https://doi.org/10.1002/qj.49712455016, 1998.

Serva, F., Cagnazzo, C., Christiansen, B., and Yang, S.: The influence of ENSO events on the stratospheric QBO in a multi-model ensemble, Climate Dynamics, 54, 2561–2575, https://doi.org/10.1007/s00382-020-05131-7, 2020.

Simpson, I. R., Shepherd, T. G., and Sigmond, M.: Dynamics of the lower stratospheric circulation response to ENSO, J. Atmos. Sci., 68, 2537–2556, https://doi.org/10.1175/JAS-D-11-05.1, 2011.

Sullivan, S. C., Schiro, K. A., Stubenrauch, C., and Gentine, P.: The response of tropical organized convection to El Niño warming, J. Geophys. Res.-Atmos., 124, 8481–8500, https://doi.org/10.1029/2019JD031026, 2019.

Taguchi, M.: Observed connection of the stratospheric quasi-biennial oscillation with El Niño–Southern Oscillation in radiosonde data, J. Geophys. Res., 115, D18120, https://doi.org/10.1029/2010JD014325, 2010.

Trepte, C. R. and Hitchman, M. H.: Tropical stratospheric circulation deduced from satellite aerosol data, Nature, 355, 626–628, https://doi.org/10.1038/355626a0, 1992.

Tsuda, T., Ratnam, M. V., Alexander, S. P., Kozu, T., and Takayabu, Y.: Temporal and spatial distributions of atmospheric wave energy in the equatorial stratosphere revealed by GPS radio occultation temperature data obtained with the CHAMP Satellite during 2001–2006, Earth Planets Space, 61, 525–533, https://doi.org/10.1186/BF03353169, 2009.

Wallace, J., Panetta, R., and Estberg, J.: Representation of the equatorial stratospheric quasi- biennial oscillation in EOF phase space, J. Atmos. Sci., 50, 1751–1762, https://doi.org/10.1175/1520-0469(1993)050<1751:ROTESQ>2.0.CO;2, 1993.

1195   Watanabe, S., Kawatani, Y., Tomikawa, Y., Miyazaki, K., Takahashi, M., and Sato, K.: General aspects

1196   of a T213L256 middle atmosphere general circulation model, J. Geophys. Res.-Atmos., 113,

1197   D12110, https://doi.org/10.1029/2008JD010026, d12110, 2008.

1198   Wang, C., Deser, C., Yu, J.-Y., DiNezio, P., and Clement, A.: El Niño–Southern Oscillation (ENSO): A

1199   review. In Reefs of the Eastern Pacific, Springer Sci. Publish., 85–106, https://doi.org/10.1007/978-

1200   94-017-7499-4_4, 2016.

1201   Xu, J.-S., On the relationship between the stratospheric quasi-biennial oscillation and the tropospheric

1202   southern oscillation, J. Atmos. Sci., 49, 725–734, https://doi.org/10.1175/1520-

1203   0469(1992)049<0725:OTRBTS>2.0.CO;2, 1992.

1204   Yoden, S., Kumar, V., Dhaka, S., and Hitchman, M.: Global monsoon systems and their modulation by

1205   the equatorial Quasi-Biennial Oscillation, MAUSAM, 74, 239–252,

1206   https://doi.org/10.54302/mausam.v74i2.5948, 2023.

1207   Yoo, C. and Son, S.-W.: Modulation of the boreal wintertime Madden-Julian oscillation by the

1208   stratospheric quasi-biennial oscillation, Geophys. Res. Lett., 43, 1392–1398,

1209   https://doi.org/10.1002%2F2016GL067762, 2016.

1210   Yu, J.-Y. and Mechoso, C. R.: A coupled atmosphere–ocean GCM study of the ENSO, J. Climate,

1211   14, 2329–2350, https://doi.org/10.1175/1520-0442(2001)014%3C2329:ACAOGS%3E2.0.CO;2,

1212   2001.

1213   Yuan, W., Geller, M. A., and Love, P. T.: ENSO influence on QBO modulations of the tropical

1214   tropopause, Q. J. Roy. Meteorol. Soc., 140, 1670–1676, https://doi.org/10.1002/qj.2247, 2014.

1215   Zawodny, J. M. and McCormick, M. P.: Stratospheric Aerosol and Gas Experiment II measurements of

1216   the quasi-biennial oscillations in ozone and nitrogen dioxide, J. Geophys. Res., 96, 9371– 9377,

1217   http://dx.doi.org/10.1029/91JD00517, 1991.

1218   Zhao, Y. and Sun, D.-Z.: ENSO asymmetry in CMIP6 models, J. Climate, 5555–5572,

1219   https://doi.org/10.1175/JCLI-D-21-0835.1, 2022.

1220   Zhang, C.: Large-scale variability of atmospheric deep convection in relation to sea surface temperature

1221   in the tropics, J. Climate, 6, 1898–1913, https://doi.org/10.1175/1520-

1222   0442(1993)006<1898:LSVOAD>2.0.CO;2, 1993.

1223

Table 1 The model configurations and respective ensemble simulations

Model configuration	Simulation	CMIP6 archive tag	Period	Ensemble size	Ensemble name
AMIP–OMA–SP	Historical AMIP	N/A	1850–2014	5	E1
AMIP–OMA–AP	Historical AMIP	N/A*	1850–2014	4	E2
Coupled–NINT–SP	CMIP6 Historical	N/A	1850–2014	5	E3
Coupled–NINT–AP	CMIP6 Historical	E2-2-G.historical.r[1-5]i1p1f1	1850–2014	5	E4

*E2-2-G.amip.r[1-5]i1p3f1 in the CMIP6 archive are the outputs of the same model but range from 1979 to 2014.

1224

Table 2 The ENSO influence on the QBO period

Member		r1			r2			r3			r4			r5		
ENSO Phase		EL	LA	EL–LA	EL	LA	EL–LA	EL	LA	EL–LA	EL	LA	EL–LA	EL	LA	EL–LA
Period (month)	E1	31.1	34.0	*(−2.9)*	34.9	35.9	−1.0	29.4	32.9	−3.5	29.7	36.7	*(−7.0)*	30.5	35.7	*(−5.2)*
	E2	33.1	36.5	*(−3.4)*	31.5	35.6	*(−4.1)*	32.1	35.4	−3.2	29.4	36.8	*(−7.4)*	n/a	n/a	n/a
	E3	27.5	33.7	−6.2	28.0	30.5	−2.5	30.5	29.8	0.7	30.0	31.5	−1.5	28.2	32.0	−3.8
	E4	31.2	35.0	*(−3.8)*	29.8	32.4	*(−2.6)*	29.7	35.4	*(−5.7)*	28.0	34.7	*(−6.7)*	28.0	33.4	*(−5.4)*

E[1-4] denote the ensemble simulations AMIP-OMA-SP, AMIP-OMA-AP, Coupled-NINT-SP, and Coupled-NINT-AP, respectively. r[1-5] indicate the ensemble members of those simulations. EL and LA are short for El Niño than during La Niña, respectively. The numbers in parentheses denote being statistically significantly different from zero at the 5% significance level.

1225

1226

1227

1228

1229

1230

1231

1232

1233

1234

1235

1236
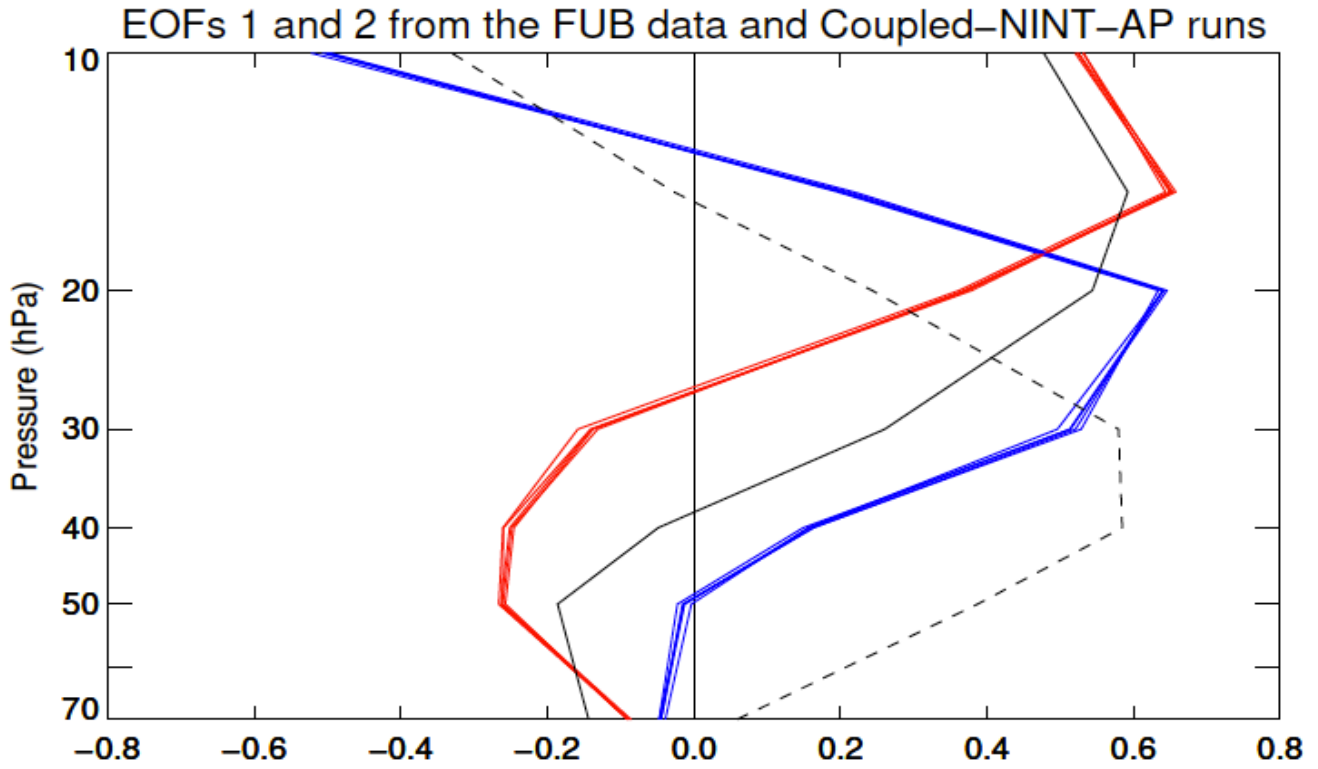
1237 **Fig. 1**. Black lines depict the first (solid) and second (dashed) orthonormal eigenvectors derived from
1238 the monthly FUB zonal wind anomalies between 1953 and 2015. Colored lines delineate the first (red)
1239 and second (blue) orthonormal eigenvectors derived from the deseasonalized and smoothed equatorial
1240 zonal mean zonal winds between 1873 and 2013 from the five Coupled–NINT–AP runs.
1241
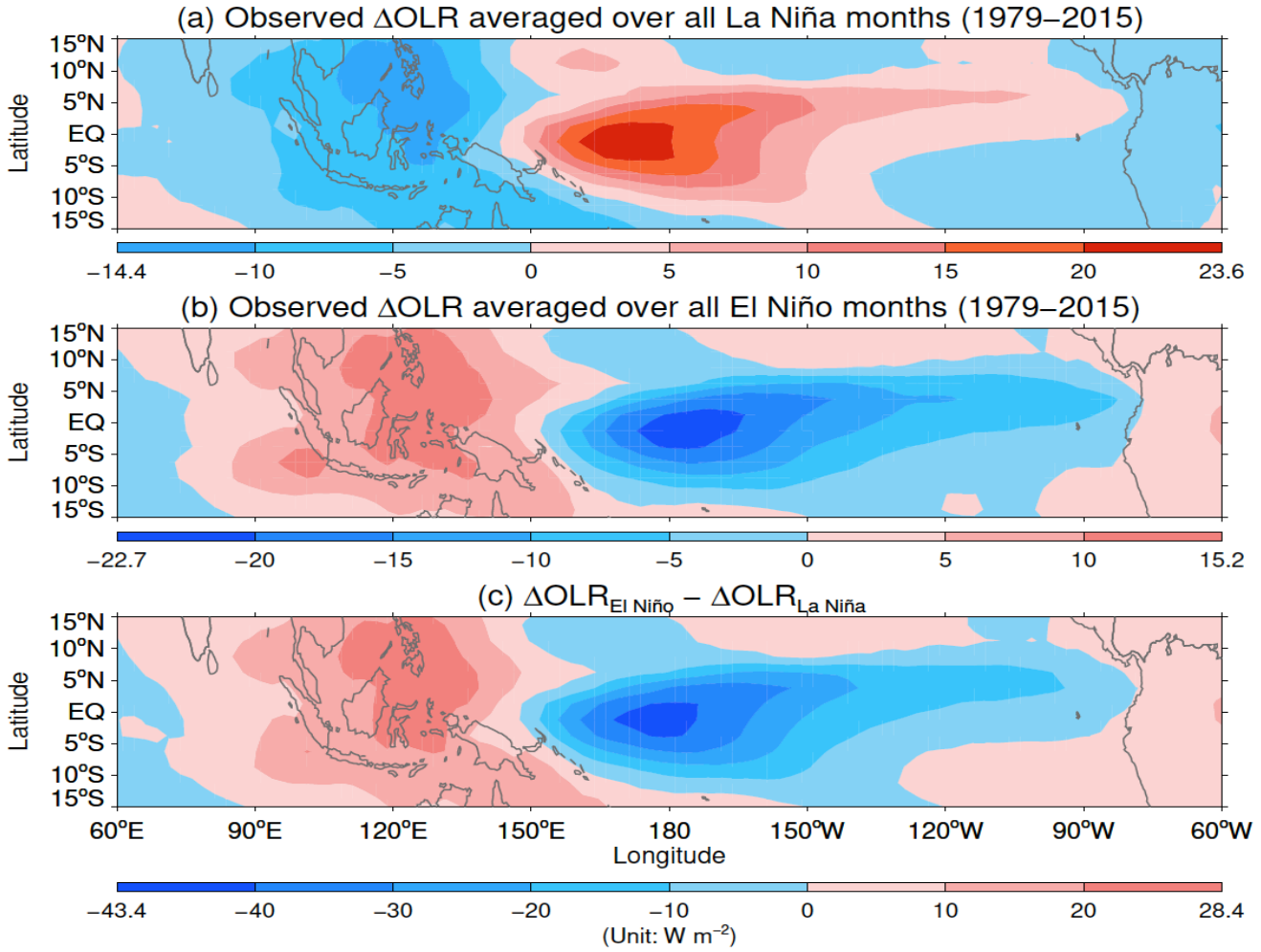
Fig. 2. Mean OLR deviations from climatology for (a) La Niña and (b) El Niño conditions over the tropical Indian and Pacific oceans. (c) Differences of mean OLRA between El Niño and La Niña conditions. The mean composite OLRA and their differences are derived from the datasets provided by NOAA NCEI.
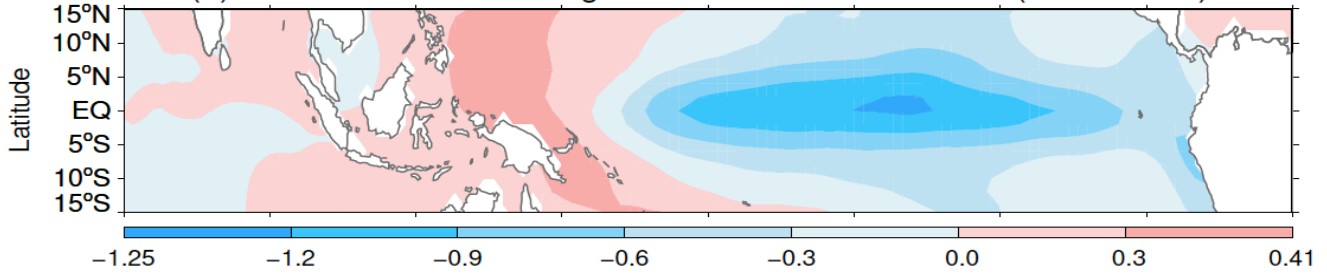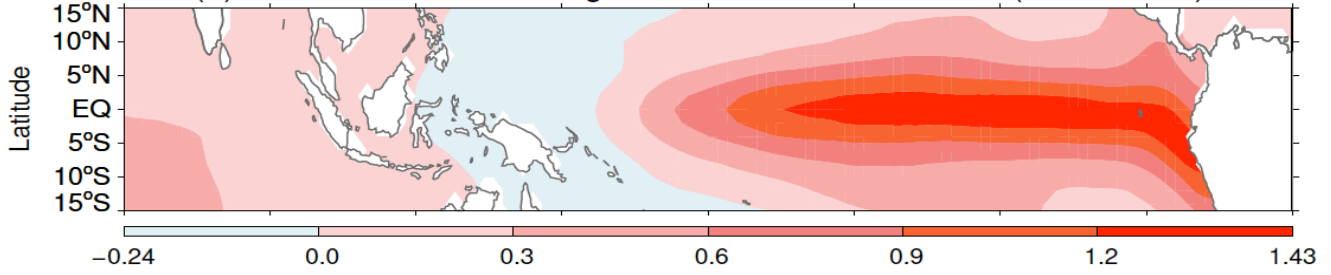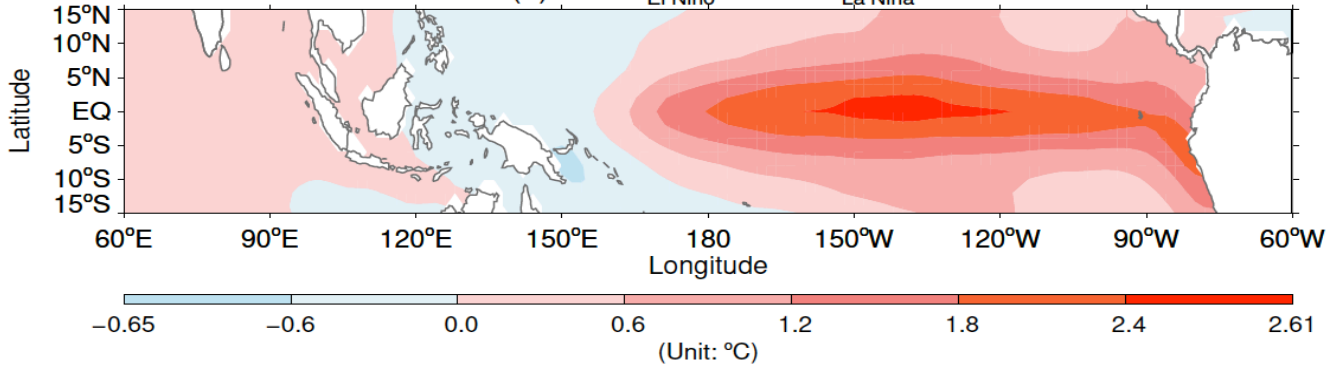
Fig. 3. Mean SST deviations from climatology for (a) La Niña and (b) El Niño conditions over the tropical Indian and Pacific oceans. (c) Differences of mean SSTA between El Niño and La Niña conditions. The mean composite SSTA and their differences are derived from the NOAA ERSSTv5 SST.
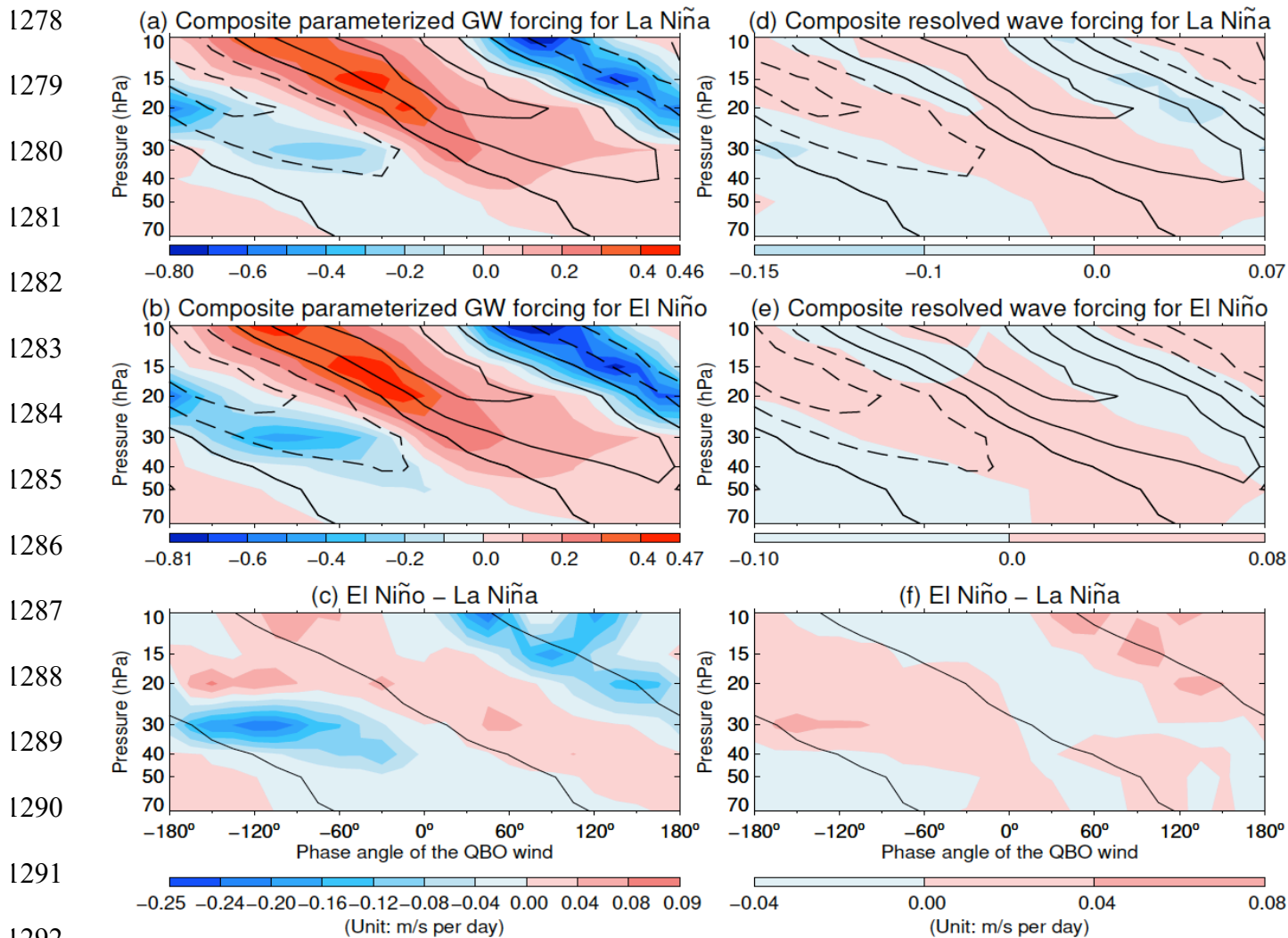
Fig. 4. Ensemble average of the composite QBO winds simulated by the Coupled–NINT–AP model during La Niña (upper panels) and El Niño (middle panels) is depicted by black contour lines where the contour interval is 10 m s⁻¹ with dashed lines denoting negatives and solid lines denoting positives and zero. The location of strong shear zones of the QBO winds during ENSO extremes is delineated by the zero wind contour lines in lower panels. For color filled contours, left panels depict the ensemble average of the composite parameterized GW forcing simulated by the Coupled–NINT–AP model averaged from 5°S to 5°N during La Niña (a) and El Niño (b) and its composite difference between El Niño and La Niña (c); right panels depict the ensemble average of the composite resolved wave forcing simulated by the Coupled–NINT–AP model during La Niña (d) and El Niño (e) and its composite difference between El Niño and La Niña (f).
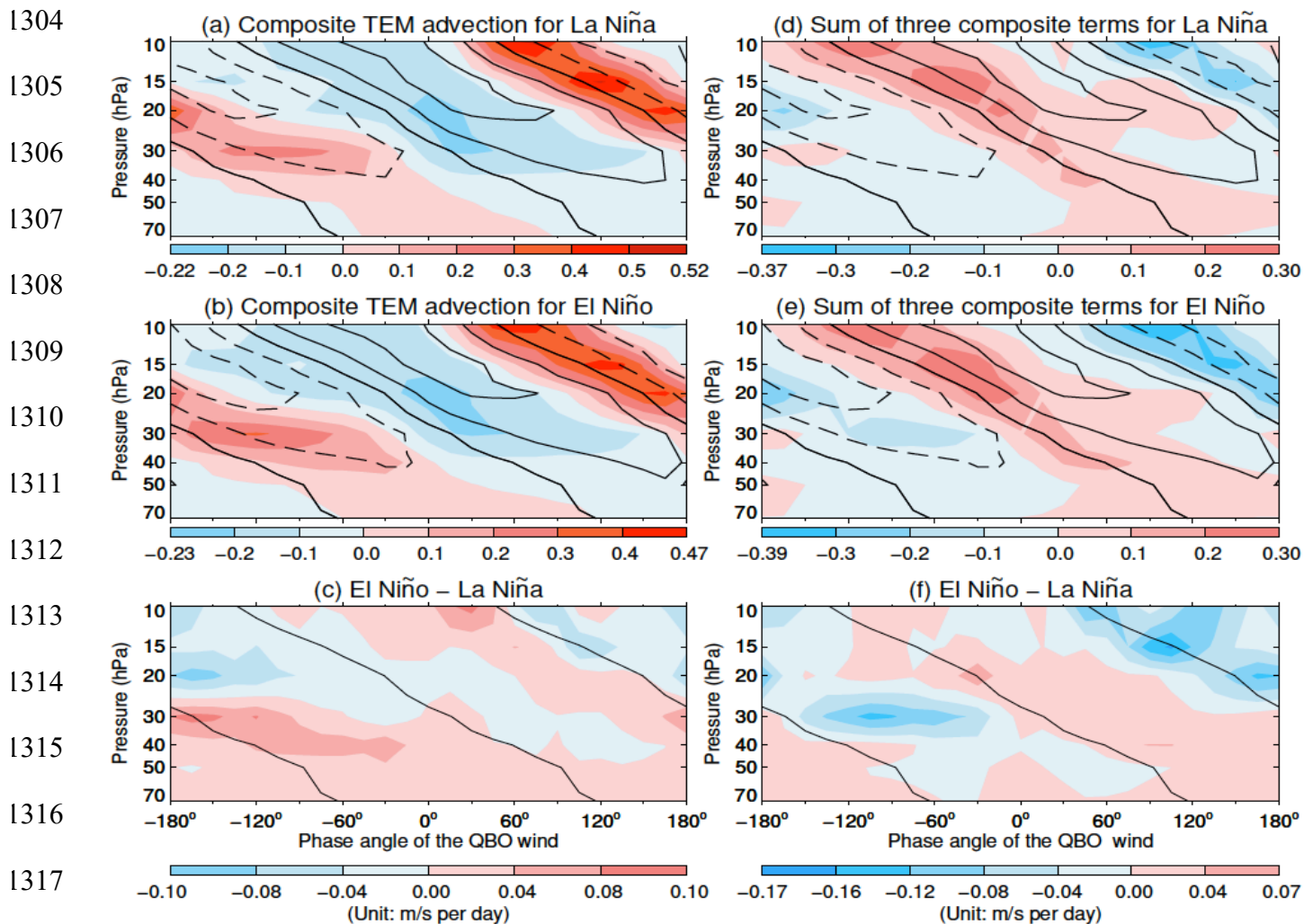
Fig. 5. The black contour lines are the same as those in Fig. 4. For color filled contours, left panels depict the ensemble average of the composite TEM advection simulated by the Coupled–NINT–AP model averaged from 5°S to 5°N during La Niña (a) and El Niño (b) and the composite difference between El Niño and La Niña (c); right panels depict the ensemble mean totaling of the composite fields of GW forcing, resolved wave forcing, and TEM advection simulated by the Coupled–NINT–AP model during La Niña (d) and El Niño (e) and the composite difference between El Niño and La Niña (f).

1325

1326

1327

1328

1329

1330

1331

1332

1333

1334

1335
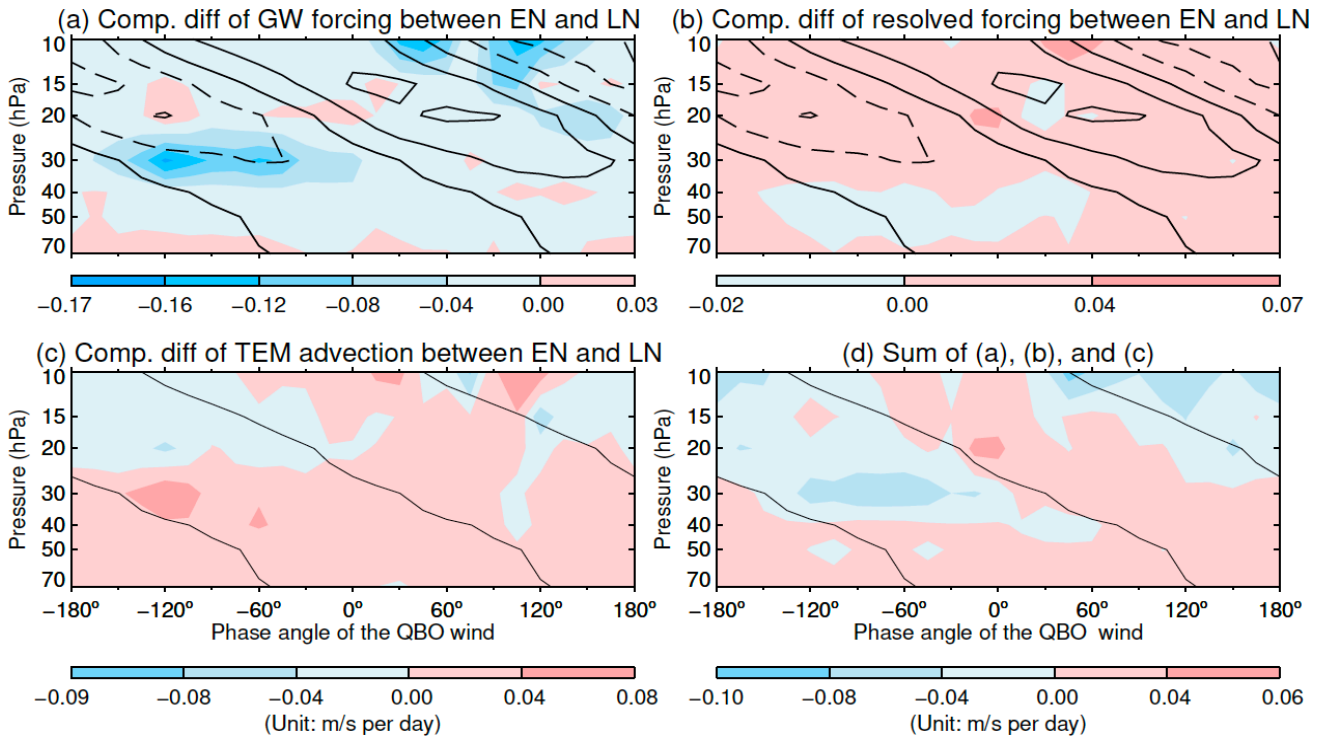
1336 **Fig. 6**. (a) and (b) are the same as the bottom panels in Fig. 4 except for the Coupled–NINT–SP model.
1337 (c) and (d) are the same as the bottom panels in Fig. 5 except for the Coupled–NINT–SP model.
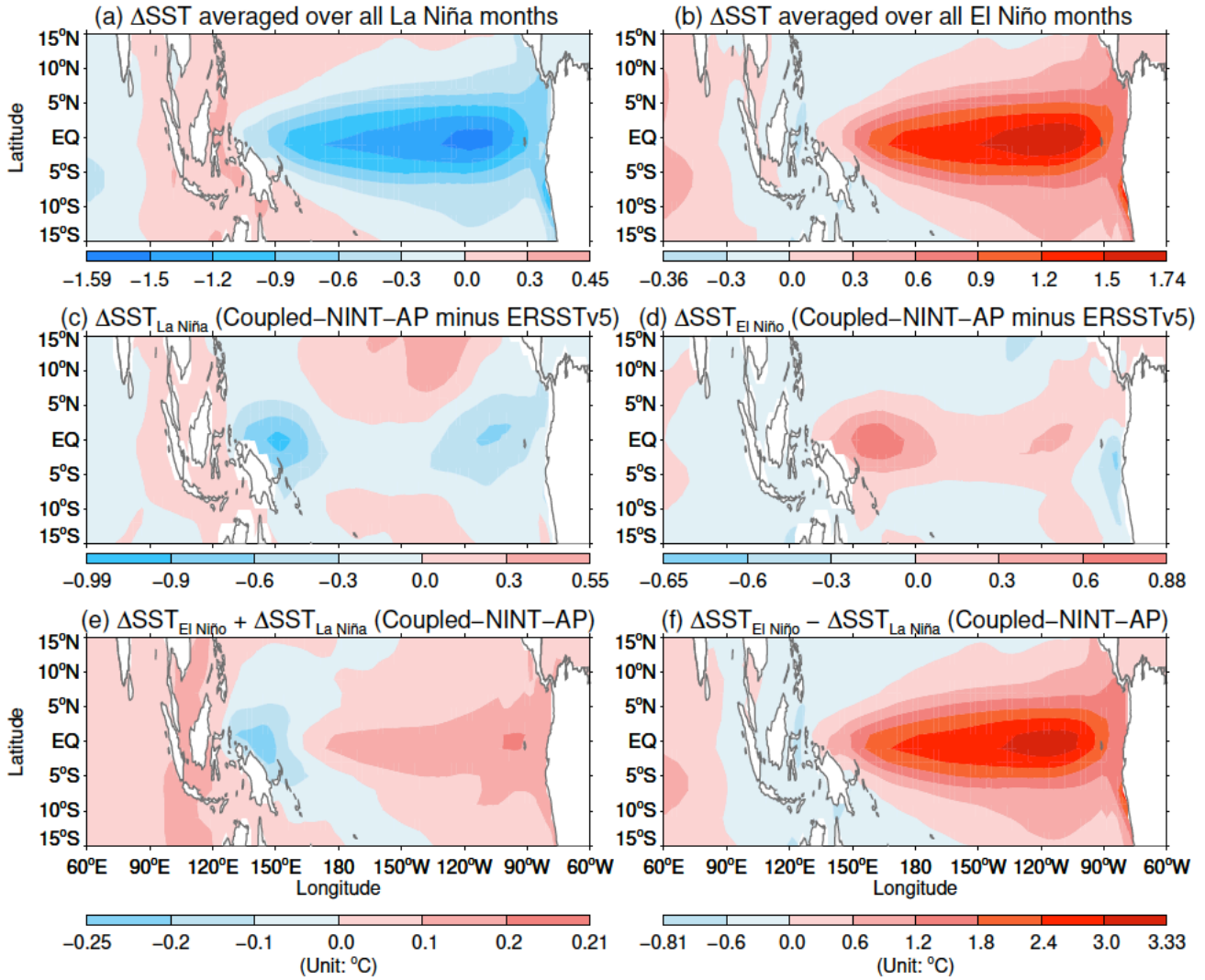
Fig. 7. Ensemble mean of the composite SSTA from the Coupled–NINT–AP runs averaged over all La Niña (a) and El Niño (b) months respectively over the 1871–2013 period. . Differences from observations are shown in (c) and (d). The sum and difference of model derived El Niño and La Niña SSTA are shown in (e) and (f), respectively.
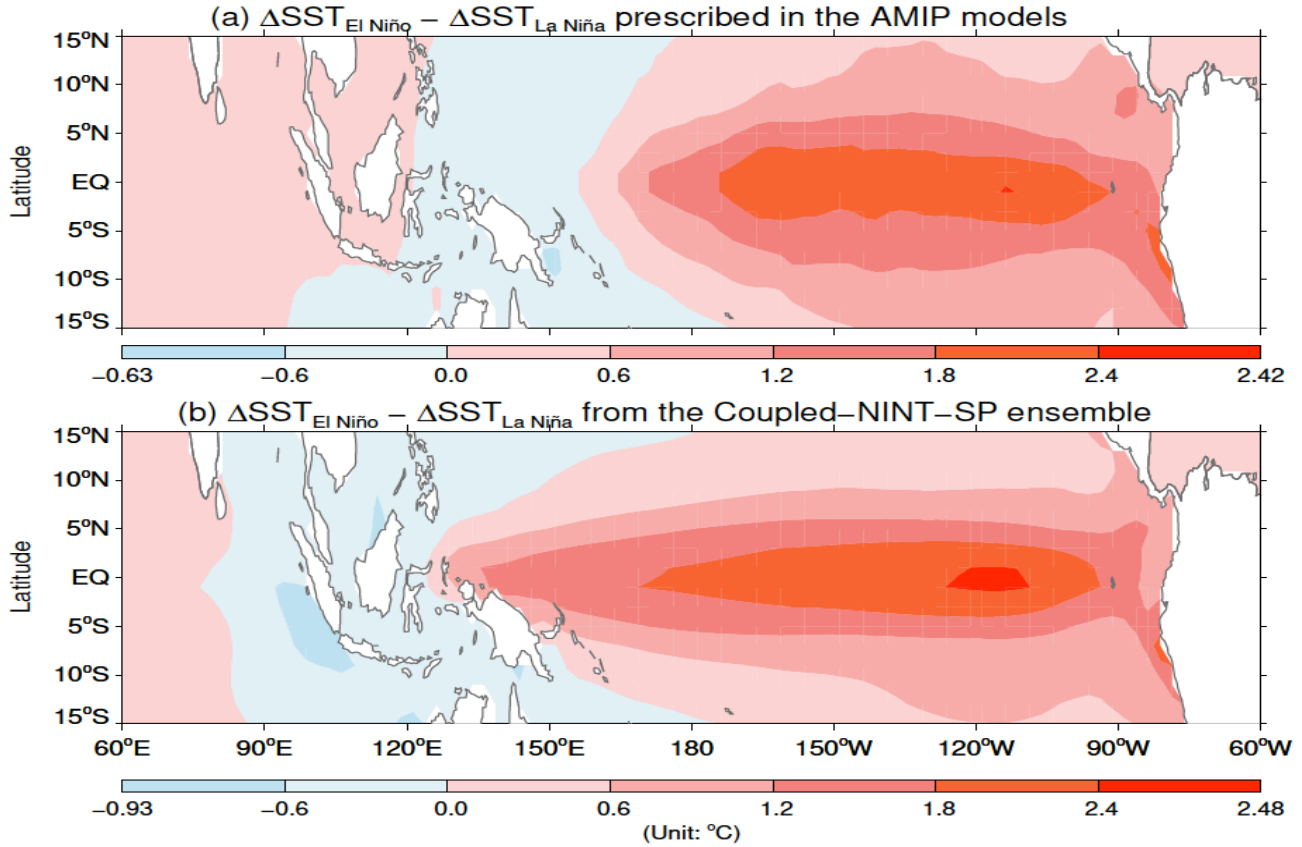
Fig. 8. Difference in the composite SSTA between El Niño and La Niña over the 1871–2013 period specified in the AMIP–OMA–SP and AMIP–OMA–AP models (a) and that simulated by the Coupled–NINT–SP model (b).
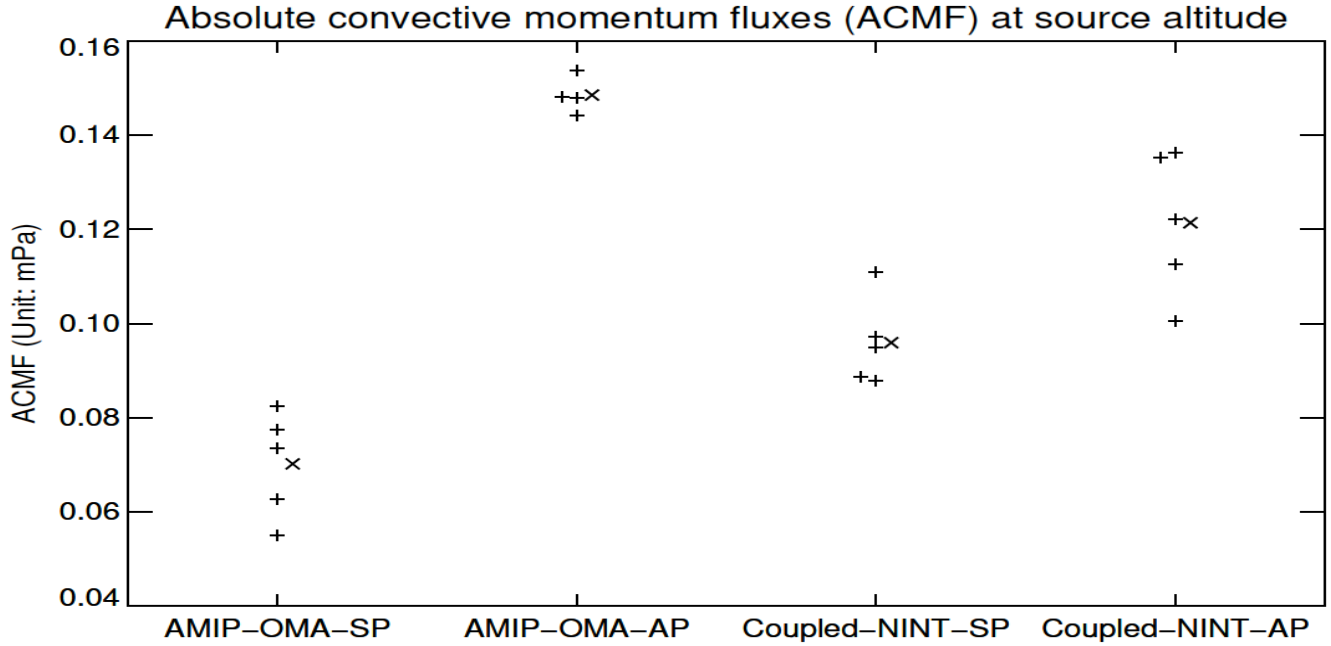
Fig. 9. Difference in the composite ACMF anomalies at the source altitude averaged over the 5°S − 5°N latitudinal belt between El Niño and La Niña over the 1871–2013 period. Plus symbol (+) denotes the difference from individual runs while cross symbol (×) represents each ensemble mean difference. Some symbols are slightly shifted leftward or rightward to avoid overlapping with other symbols.
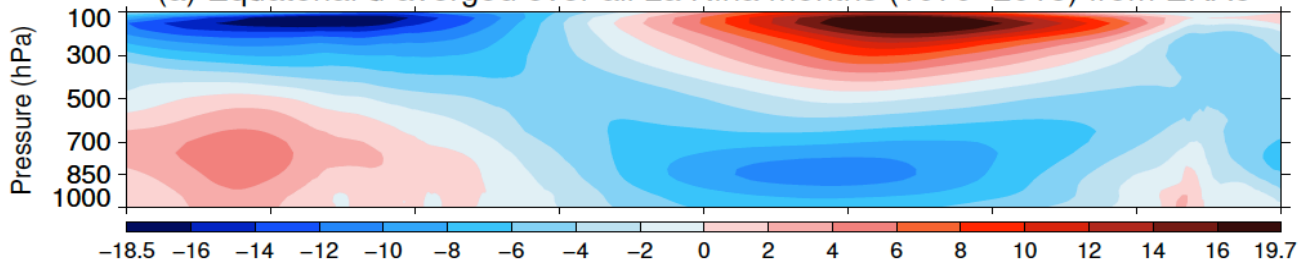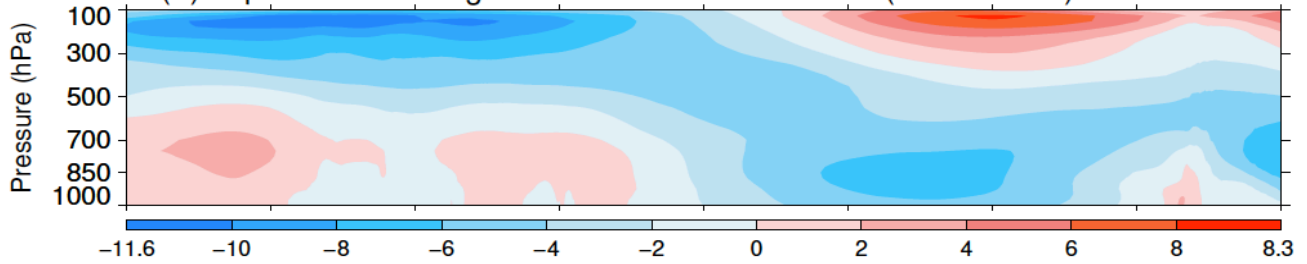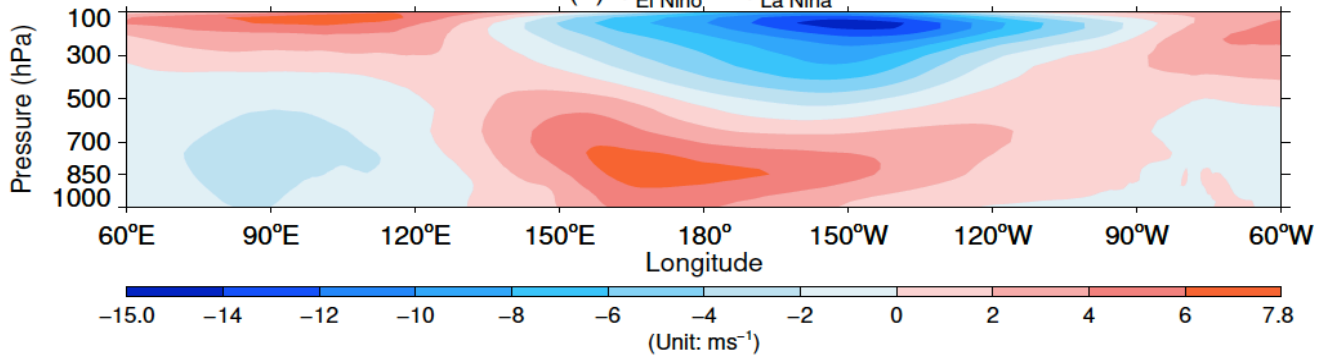
Fig. 10. Zonal winds from ERA5 averaged from 5°S to 5°N that are further averaged over all La Niña (a) and El Niño (b) months between 1979 and 2015 respectively, and their differences (c).

1404

1405

1406

1407

1408

1409

1410

1411

1412

1413
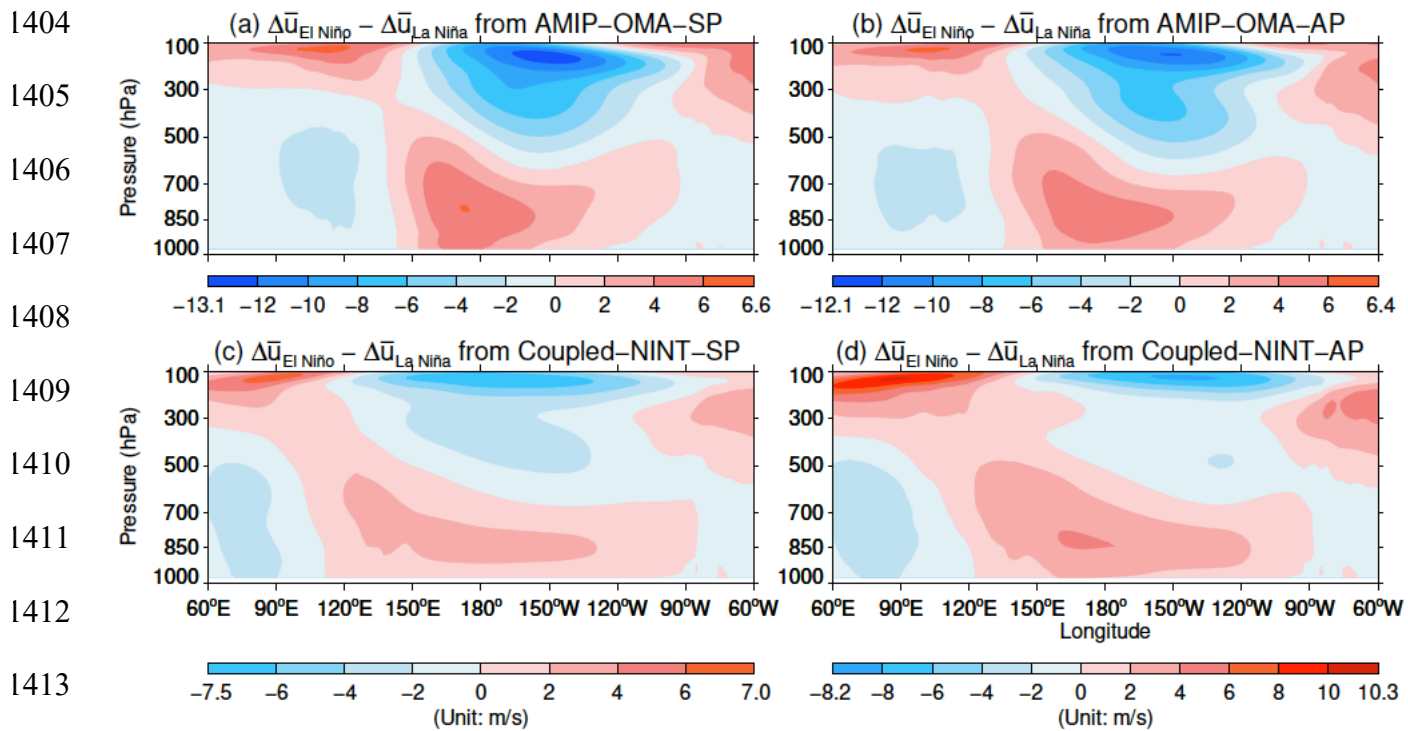
1414 **Fig. 11**. Same as Fig. 10c but for the ensemble averages of the composite difference in zonal wind
1415 anomalies between El Niño and La Niña simulated by AMIP–OMA–SP (a), AMIP–OMA–AP (b),
1416 Coupled–NINT–SP (c), and Coupled–NINT–AP (d).
1417
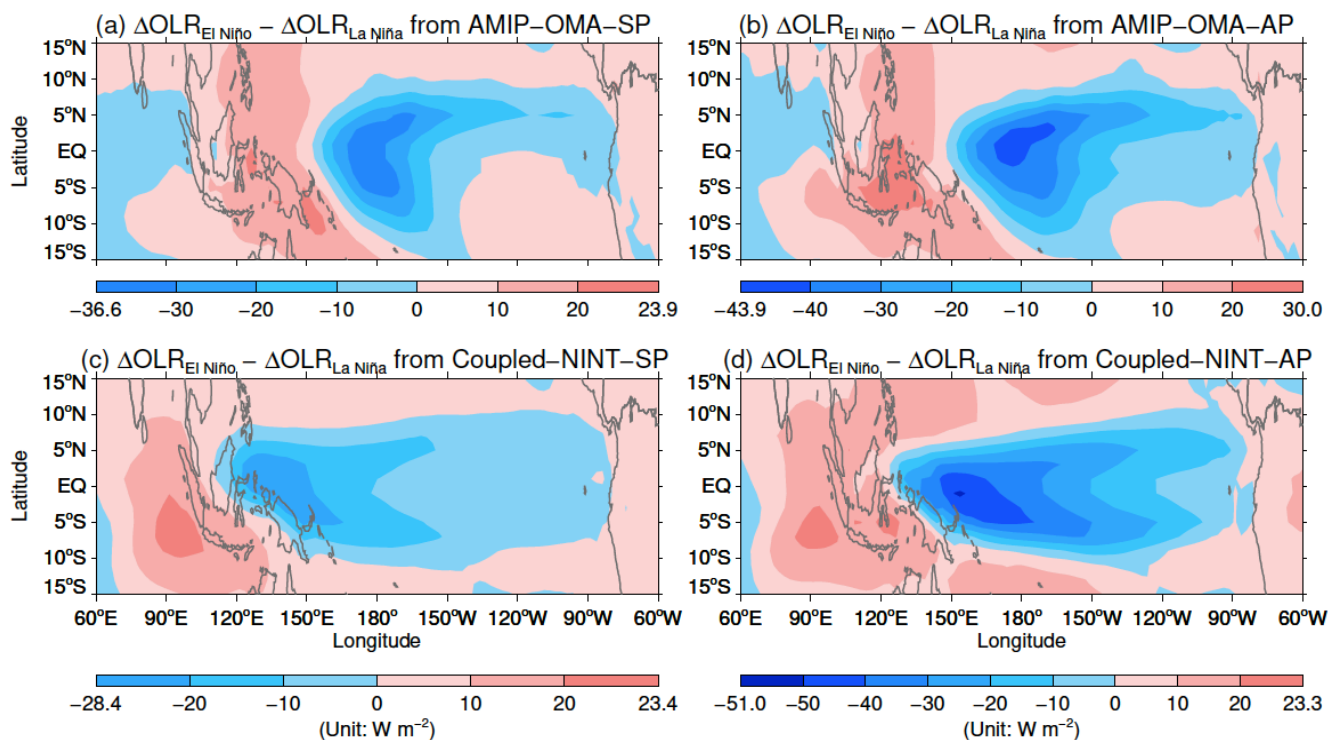
Fig. 12. Same as Fig. 11 but for the ensemble averages of the composite difference in OLRA between El Niño and La Niña simulated by AMIP–OMA–SP (a), AMIP–OMA–AP (b), Coupled–NINT–SP (c), and Coupled–NINT–AP (d).

1432

1433

1434

1435

1436

1437

1438

1439

1440
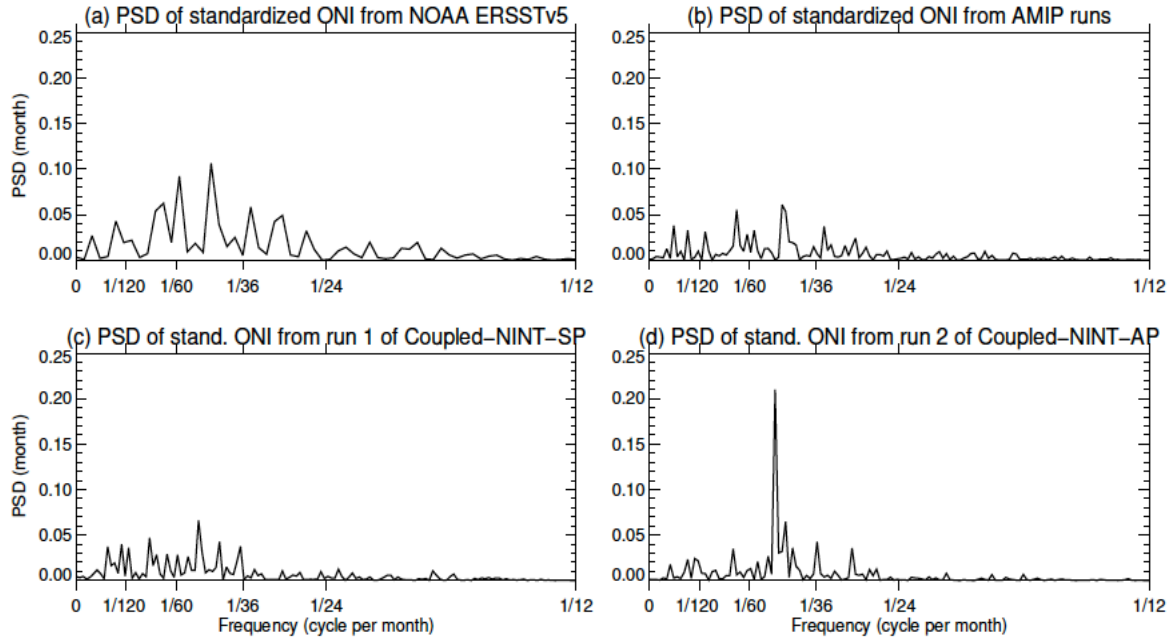
1441 **Fig. 13**. Power spectral densities (PSD) of the standardized ONI between 1953 and 2015 derived from
1442 the NOAA ERSSTv5 SST (a), of standardized ONI between 1871 and 2013 derived from the HadISST1
1443 dataset as used in the AMIP runs (b), of standardized ONIs between 1871 and 2013 simulated by the
1444 first realization of Coupled–NINT–SP (c) and the second realization of Coupled–NINT–AP (d),
1445 respectively.

1446